A sensitivity analysis of twinning crystal plasticity finite element model using single crystal and poly crystal Zircaloy

Shank S. Kulkarni[a,b,*], Aditya Venkatraman[a], David J. Senor[a], Ram Devanathan[a]

[a] *Pacific Northwest National Laboratory, Richland, WA 99354, USA*
[b] *The University of Tennessee, Knoxville, TN 37996, USA*

Abstract

The popularity of crystal plasticity finite element method (CPFEM) models is increasing due to their ability to predict the mechanical response of crystalline materials such as metals and metal alloys more accurately than traditional continuum mechanics models. This is since the crystal plasticity models consider the effect of atomic structure, microstructural morphology, and properties of individual grains. These CPFEM models use a large number of material parameters in order to capture the mesoscale physics which comes with the downside of the tedious calibration process. In this paper, a CPFEM code was developed to include the twinning induced grain reorientation and subsequent crystallographic slip for HPC material. The developed code is incorporated in a large-scale, parallelized nonlinear solver WARP3D. A sensitivity analysis with respect to 22 material parameters was then conducted using single crystal and polycrystal representative volume element (RVE) of Zircaloy material. Loading was applied along five different crystallographic orientations for single crystal RVE and along three directions namely, rolling (RD), transverse (TD), and normal (ND) direction for polycrystal RVE. Results obtained from the sensitivity analysis were used for the calibration of material parameters for Zircaloy. Finally, developed code along with calibrated material parameters was used to investigate the effect of the hydride phase formation in Zircaloy which is a typical case observed for nuclear applications. It was found that the volume fraction of the hydride phase has a significant impact on the mechanical properties of Zircaloy.

Keywords: crystal plasticity, finite element analysis, CPFEM, twinning, Zircaloy, hydrides, sensitivity analysis, WARP3D

1. Introduction

Crystalline materials such as metals and metallic alloys are one of the most widely used classes of materials in multiple applications for centuries. They have some extremely useful properties such as

*Corresponding author
Email address: skulka10@utk.edu/shankkulkarni1316@gmail.com (Shank S. Kulkarni)

high strength, ductility, toughness, and conductivity to name a few. Metals and metallic alloys can be reshaped into any complex geometry either by melting them or just by plastically deforming them at elevated temperatures. Hence it is crucial to understand the mechanical response of metals to different types of loading and create mathematical models which can predict that response accurately. The main challenge in developing such mathematical models is the anisotropic behavior of crystalline materials which is directly related to the microstructure and atomic structure of the material. The degree of anisotropy is usually dependent on many parameters such as manufacturing technique, size of the component, grain size, and atomic structure. But, it is widely accepted that the overall deformation of a poly-crystalline material is highly dependent on the microstructural morphology and properties of individual grains [1, 2, 3]. Crystal plasticity (CP) constitutive models consider these factors while predicting the mechanical response of the crystalline materials. The foundation of crystal plasticity theory was laid in the early '30s by Taylor and Schmid [4] followed by a mathematical model developed by Needleman [5]. In CP constitutive models, the total deformation of the material is divided into two parts: elastic and plastic. The elastic deformation component is modeled using the stretching of the crystalline lattice of the material whereas the plastic deformation component is modeled using slip (motion of dislocation through crystal lattice) or twin (symmetrical intergrowths of crystals). Further, the rate of evolution of the plastic part of the deformation is specified as a superposition of slip and twinning in the component slip systems, which are defined by a slip plane normal and slip direction. The utilization of crystal plasticity models to evaluate the slip and twin activity in HCP metals is quite challenging compared to FCC or BCC metals due to the prevalent anisotropy in the elastic and plastic properties. More specifically, there exist multiple families that are capable of accommodating slip and twin activity in HCP metals with widely disparate critical resolved shear stress (CRSS) values required to activate them. Furthermore, deformation twinning is commonly observed in HCP metals such as Magnesium and Zirconium with a low number of active slip systems. It should be pointed out that the initiation of twinning in grain is accompanied by a crystal lattice rotation according to a fixed reflection tensor.

CP models typically need the help of numerical methods in order to solve differential equations. The finite element method (FEM) is most commonly used along with CP models due to its robust nature and ability to model complex geometries [6]. When FEM is used along with CP models, they are referred to as crystal plasticity finite element method (CPFEM) models [7]. Early CPFEM models did not explicitly model the grain morphology but rather considered a single finite element as a homogenization of multiple grains which limits them to represent the grain boundaries [8, 9]. More recent studies do model detailed, more accurate microstructure which is referred to as full-field modeling [10, 11]. Hansen et al. [12] developed a dislocation-based single crystal plasticity model and applied it to copper. The model's prediction of stress-strain curves was shown to be in good

agreement with experimental results. Ardeljan et al. [13] developed a CP model which is sensitive to temperature as well as strain rate and demonstrated its robustness by applying it to obtain a stress-strain response of AZ31 magnesium alloy. Hama et al. [14] used CPFEM to study the response of AZ31 rolled magnesium alloy sheets under two-step loading. Li et al. [15] used the CPFEM model to predict the interaction among heterogeneous deformation, dynamic recrystallization, and mechanical response of titanium alloys. Baudoin et al. [16] compared the CPFEM results of uniaxial tension tests of titanium oligocrystal with experiments and showed a good agreement between them.

Whereas deformation slip has been studied extensively in the context of crystal plasticity, the modeling of deformation twinning faces certain challenges that impede its implementation. Firstly, the reason(s) for twin inception in grains has not been conclusively established. Secondly, the specifics of slip activity in the twinned portion of the grain are still a matter of debate. However, there have been past studies that have successfully incorporated twinning in crystal plasticity models. Many of these models use the statistical criterion developed by Van Houtte et al. [17], wherein it was suggested to reorient a specified volume fraction of the grain based on the value of the accumulated twinning shear. Kalidindi et al. [18] proposed a new methodology that considered twin volume fraction accumulation as a pseudo-slip process, which can be modeled using the same schemes as deformation slip. The reorientation of the grain was affected depending on the accumulated volume fractions as estimated by the model. Salem et al. [19] followed up the study by analyzing the interaction between twinning and strain hardening and were able to successfully predict the three stage strain hardening in α-Titanium and macroscopic stress-strain curves. Abdolvand et al. [20] incorporated the Kalidindi's twinning model to simulate the evolution of lattice strains and texture in Zircaloy–2 material. Ardeljan and Knezevic [21, 22, 23] further extended the model by adding the formulation for double twinning in which a single grain can initiate two twinned regions simultaneously. Multiple sets of slip families have been considered to model deformation twinning, in addition, to slip in HCP metals. Staroselsky et al. [24] modeled the slip activity in AZ31 alloy using Basal, Prismatic, and Pyramidal <a> family of slip systems. Pyramidal <c+a> slip has also been incorporated in order to accommodate plastic straining along the c-axis in various other studies [25, 26, 27, 28]. Cheng and Ghosh [29, 30] explicitly modeled the nucleation, propagation, and growth of the twinned region in polycrystalline magnesium. Kasemer and Dawson [31] used the method of discretizing the grains into the laminar structure to explicitly model twinned regions. Yaghoobi et al. [32, 33] developed a model to simulate the twinning as well as detwinning behavior observed in the case of HCP polycrystals. Sundararaghavan et al. [34, 35] implemented crystal plasticity in the realm of peridynamics which is a newly developed non-local continuum mechanics formulation to model crack initiation and propagation [36, 37].

Although CPFEM models are still not available in any commercial FEM software, some open-source FEM codes have been incorporated with CP modules. Multiphysics Object Oriented Simulation

Environment (MOOSE) code developed by Idaho national laboratory [38] has a crystal plasticity module which was used by Grilli et al. [39] to model the residual stress in the additive manufacturing process. Similarly, a nonlinear large-scale 3-D structural mechanics finite element code WARP3D has a CP module for BCC, FCC, and HCP materials which considers plastic deformation only due to slip [40, 41]. Multiple studies have been conducted using this code previously for steel [42, 43] as well as Zircaloy [44, 45]. Some FEM codes are specifically developed for crystal plasticity such as PRISM [46] and FEPX [47]. Both codes are updated frequently and new features are added periodically. PRISM has a strong solver with multiple fatigue crystal plasticity models while FEPX has the advantage of seamless coupling with microstructure generation software Neper [48] and meshing software Gmsh [49]. Most often these CPFEM codes depend heavily on other software for pre-processing such as generating digital microstructure, creating finite element mesh, or assigning orientations, and for post-processing such as visualization. In addition to this, multiple studies developed and used their proprietary in-house codes such as Abaqus UMAT[50, 51] and JAS3D [52].

Most of the polycrystalline CPFEM simulations are performed with the help of the representative volume element (RVE) of the whole domain. This is primarily to save computational costs. Three main aspects which must be chosen carefully for any such CPFEM studies are:

1. RVE size and Mesh size
2. Type of finite elements to be used
3. CP model material parameters

Recently, Lim et al. [52] conducted a mesh sensitivity analysis and also investigated the optimum size of RVE to be used in CPFEM simulations. They found that mesh sensitivity is highly dependent on initial crystal orientations, applied boundary conditions, and the type of hardening model used. They also showed that an RVE with 1,000 grains is adequate to obtain good results for uniaxial tension loading. The effect of mesh resolution and the type of elements used in CPFEM simulation on the accuracy of results and convergence rate was studied by Feather et al. [53] in a separate study. Work presented in this manuscript complements both recent works mentioned earlier by conducting the sensitivity analysis with respect to the material parameters of the CP model. In this work the CP model which includes twinning systems was incorporated into the CP sub-modules of the open-source nonlinear FE solver WARP3D. The motivation behind this implementation is to explain the process of adding any material model into the modular code of WARP3D. Readers can use this to implement the material model of their interest (not limited to the CP model) with ease by referring to the details given in this paper. In order to understand the effect of each material parameter, a detailed sensitivity analysis was conducted. The results of sensitivity analysis can be used to calibrate the material parameters

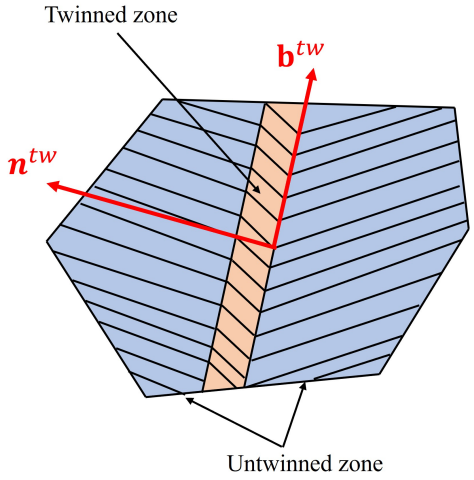

Figure 1: Twinned and an untwinned portion of grain separated by a twin plane.

for the CPFEM model for any other material with the use of stress-strain curves. Calibration was then conducted using three experimental uniaxial stress-strain curves of Zircaloy-2 given by [54]. As a case study, an RVE of Zircaloy material with heterogeneities of zirconium hydride was modeled to understand the effect of hydride volume fraction on the overall mechanical properties of the RVE.

This paper is outlined as follows: section 1 provides the introduction of the topic along with the motivation behind this work. Section 2 provides the detailed theoretical background of the crystal plasticity model considering deformation due to twin. Next, section 3 gives the details of implementing the CP model in FEM code WARP3D. Section 4 provides the discussion on the single crystal as well as polycrystal results obtained using implemented CPFEM model. The following section 5 provides the results of sensitivity analysis conducted for single as well as polycrystalline RVE of Zircaloy material. Section 6 discusses the case study conducted using the implemented CPFEM model where the effects of hydride volume fraction in the Zircaloy matrix on the mechanical properties of RVE were studied. Finally, section 7 provides the concluding remarks. Manuscript concludes with the summary of code changes to WARP3D software presented in Appendix A.

2. Theoretical background

Figure 1 illustrates a single grain with a twinned zone that is separated from the untwinned zone by a twin plane with twin normal $\boldsymbol{n}^{tw}$. The rate of evolution of the plastic part of the deformation gradient $\boldsymbol{L}^{p}$ should account for the slip in the parent grain, twin volume fraction evolution, and slip

in the twinned region, and is expressed in the lattice frame as follows [18]:

$$\begin{aligned}
\boldsymbol{L}^p =& \boldsymbol{\Omega}^p + \boldsymbol{D}^p, \quad \text{where,} \\
\boldsymbol{D}^p =& (1 - \sum_{\beta=1}^{N_{tw}} f^\beta) \sum_{\alpha=1}^{N_s} \dot{\gamma}^\alpha \tilde{\boldsymbol{m}}^\alpha + \sum_{\beta=1}^{N_{tw}} (f^\beta \sum_{\alpha=1}^{N_{s_t}} \dot{\gamma}^\alpha \tilde{\boldsymbol{m}}^\alpha) + \sum_{\beta=1}^{N_{tw}} \dot{f}^\beta \gamma_0^{tw} \tilde{\boldsymbol{m}}_{tw}^\beta, \\
\boldsymbol{\Omega}^p =& (1 - \sum_{\beta=1}^{N_{tw}} f^\beta) \sum_{\alpha=1}^{N_s} \dot{\gamma}^\alpha \tilde{\boldsymbol{q}}^\alpha + \sum_{\beta=1}^{N_{tw}} (f^\beta \sum_{\alpha=1}^{N_{s_t}} \dot{\gamma}^\alpha \tilde{\boldsymbol{q}}^\alpha) + \sum_{\beta=1}^{N_{tw}} \dot{f}^\beta \gamma_0^{tw} \tilde{\boldsymbol{q}}_{tw}^\beta,
\end{aligned} \tag{1}$$

where $\tilde{\boldsymbol{m}}^\alpha$ and $\tilde{\boldsymbol{q}}^\alpha$ represent the symmetric and skew-symmetric parts of the Schmid tensor expressed in the lattice frame, $\dot{\gamma}^\alpha$ is shear rate in slip system α, f is the volume fraction of twinned region, γ_0^{tw} is constant shear strain associated with twinning, and N_s, N_{tw}, N_{s_t} represent the number of slip systems in the parent grain, the number of twinning systems, and the number of slip systems in the child grain respectively. In this current model, slip/twin shear rate evolution is specified according to a flow - rule [55]:

$$\dot{\gamma}^\alpha = \dot{\gamma}_0 \left(\frac{|\tau^\alpha|}{g^\alpha} \right)^{1/m} \text{sgn}(\tau^\alpha), \tag{2}$$

where $\dot{\gamma}_0$ is reference plastic shearing rate, m is material constant, g^α is strength of slip/twin system α, τ^α is resolved shear stress on the slip/twin system α, and $sgn()$ is a sign function. The rate of slip/twin volume fraction depends on the resolved shear stress on each slip/twin system as well as the critical resolved shear stress (CRSS) required to activate slip activity in that slip system. In addition, the twin volume fraction is related to the accumulated pseudo-slip on the twin systems as [18]

$$\begin{aligned}
\dot{f}^\beta =& \frac{\dot{\gamma}^\beta}{\gamma_0^{tw}}, \quad f^\beta \geq 0, \quad \sum_\beta f^\beta \leq 1, \text{if} \quad \tau^\beta \geq 0, \\
\dot{f}^\beta =& 0, \text{if} \quad \tau^\beta \leq 0.
\end{aligned} \tag{3}$$

The rate-sensitivity parameter is usually set to a high value to inhibit excess rate dependency at room temperature.

The objective rate of change of stress used in this formulation is the Brown-Naghdi stress rate specified in the unrotated configuration. The resolved shear stress is specified as

$$\tau^\alpha = \boldsymbol{\sigma} : \boldsymbol{R}^{pT} \tilde{\boldsymbol{m}}^\alpha \boldsymbol{R}^p, \tag{4}$$

where $\boldsymbol{\sigma}$ is Cauchy stress.

The spin and pure stretch parts of the plastic stretching tensor $\boldsymbol{L}^p$ are pushed to the intermediate unrotated configuration using the plastic rotation tensor. This allows the specification of the Brown-Naghdi Objective stress rate in that configuration as follows:

$$\dot{\boldsymbol{\sigma}} = \underline{\underline{\mathbf{C}}} : (\boldsymbol{D} - \bar{\boldsymbol{D}}_p) + \boldsymbol{R}\bar{\boldsymbol{w}}^p \boldsymbol{R}^T \boldsymbol{\sigma} - \boldsymbol{\sigma} \boldsymbol{R}\bar{\boldsymbol{w}}^p \boldsymbol{R}^T, \tag{5}$$

where $\boldsymbol{D}$ is the total deformation rate, $\bar{\boldsymbol{D}}_p$ is pure stretch part plastic stretching tensor $\boldsymbol{L}^p$, $\bar{\boldsymbol{w}}^p$ is the plastic vorticity within correction terms accounting for plastic rotation, and $\underline{\underline{\mathbf{C}}}$ is the fourth-order elastic stiffness tensor. The hardening variables (specifically, the CRSS values) are assumed to evolve with accumulated shear strains in the slip and twinning systems.

For Zircalloy-2, Abdolvand et al. [20] utilized an extended Voce hardening law, that is expressed as

$$g^\alpha = g_0^\alpha + (g_1^\alpha + \theta_1^\alpha \Gamma)\left(1 - \exp\left(\frac{-\theta_0^\alpha \Gamma}{g^\alpha}\right)\right), \tag{6}$$

where g_0^α is the initial CRSS of the slip/twin system, θ_0^α is the initial hardening rate, and g_1^α and θ_1^α determine the large-strain hardening behavior, and $\Gamma = \sum_\beta \int |\dot{\gamma}^\beta| dt$ is the accumulated shear strain on all slip/twin slip systems. The evolution of the CRSS can be calculated by differentiating Eq. (6), and the terms in the hardening matrix can be calculated. The evolution equation accounts for latent hardening, in addition to self-hardening. Differentiating Eq. (6) w.r.t time, we get

$$\begin{aligned} \dot{g}^\alpha =& \frac{\partial g^\alpha}{\partial \Gamma}\frac{\partial \Gamma}{\partial t}, \\ =& q_{\alpha\beta} h_{\alpha\beta} \sum_\beta |\dot{\gamma}^\beta|, \end{aligned} \tag{7}$$

where $q_{\alpha\beta}$ is the latent hardening matrix and

$$h_{\alpha\beta} = \left\{(g_1^\alpha + \theta_1^\alpha) + \left(\theta_0^\alpha - \theta_1^\alpha + \frac{\theta_0^\alpha \theta_1^\alpha}{g_1^\alpha}\right)\exp\left(\frac{-\theta_0^\alpha \Gamma}{g^\alpha}\right) + \theta_1^\alpha \Gamma\right\}. \tag{8}$$

Eqs. (4) and (7) are coupled PDEs that are numerically solved with the help of various optimizers to advance the time-step of deformation. In addition, WARP3D requires the specification of certain derivatives to construct the material Jacobian. Specifically, it requires the derivative of the slip rate w.r.t the resolved shear stress and CRSS, and the derivative of the hardening function w.r.t itself as well as the Cauchy stress. These derivatives are calculated using the following expressions:

$$\begin{aligned} g_{n+1}^\alpha =& g_n^\alpha + \sum_\beta h_{\alpha\beta} q_{\alpha\beta} \Delta\gamma_{n+1}^\beta, \\ \frac{\partial g_{n+1}^\alpha}{\partial g_{n+1}^\beta} =& h_{\alpha\beta} q_{\alpha\beta} \frac{\partial \Delta\gamma_{n+1}^\beta}{\partial g_{n+1}^\beta} = -\frac{h_{\alpha\beta} q_{\alpha\beta} \dot{\gamma}_0}{m}\left(\frac{\tau_{n+1}^\beta}{g_{n+1}^\beta}\right)^{1/m-1} \frac{dt}{{g_{n+1}^\beta}^2}, \\ \frac{\partial g_{n+1}^\alpha}{\partial \boldsymbol{t}} =& \sum_\beta h_{\alpha\beta} q_{\alpha\beta} \frac{\partial \Delta\gamma_{n+1}^\beta}{\partial \boldsymbol{t}} = dt \sum_\beta \frac{h_{\alpha\beta} q_{\alpha\beta} \dot{\gamma}_0}{m}\left(\frac{\tau_{n+1}^\beta}{g_{n+1}^\beta}\right)^{1/m-1} \bar{\boldsymbol{m}}_s^\beta. \end{aligned} \tag{9}$$

3. Implementation in WARP3D

WARP3D's crystal plasticity module can consider only deformation via slip for HCP material. In this section, we describe a workflow to incorporate twin inception, twin volume fraction evolution, and calculation of slip activity in the twinned portion into the existing CP module in WARP3D. The

Elastic stiffness	$C^{ch}_{ijkl} = Q^{ip}_{tw} Q^{jq}_{tw} Q^{kr}_{tw} Q^{ls}_{tw} C^{pa}_{pqrs}$
Slip families	Basal, Prismatic, Pyramidal <c+a>
Euler angles	$\boldsymbol{g}^{ch} = \boldsymbol{Q}^{tw,T} \boldsymbol{g}^{pa} \boldsymbol{Q}^{tw}$
$\boldsymbol{m}^s, \boldsymbol{q}^s$	$\boldsymbol{m}^{s,ch} = \boldsymbol{Q}^{tw} \boldsymbol{m}^{s,pa} \boldsymbol{Q}^{tw,T}$, $\boldsymbol{q}^{s,ch} = \boldsymbol{Q}^{tw} \boldsymbol{q}^{s,pa} \boldsymbol{Q}^{tw,T}$
$\boldsymbol{\sigma}, \boldsymbol{R}^p, \boldsymbol{F}^e, \boldsymbol{d}$	Unchanged

Table 1: Changes to state variables within the twinned portion of the grain. $\boldsymbol{Q}^{tw}$ is defined in Eq. (10)

initiation of twin causes the reorientation of a portion of the parent grain as shown in Fig. 1. All material directions in the twinned zone are reflected from the twin plane in the twinned zone, as compared to the untwinned zone. This rotation can be specified using a rotation matrix $\boldsymbol{Q}^{tw}$ as

$$\boldsymbol{Q}^{tw} = 2\boldsymbol{n}^{tw} \otimes \boldsymbol{n}^{tw} - \boldsymbol{I}, \tag{10}$$

where $\boldsymbol{I}$ is the identity matrix. A new child grain is created with orientation specified by rotating the parent grain according to the rotation matrix when the condition for twinning is reached. This condition is still a matter of debate but, herein, it is specified using a critical volume fraction of 2%. The grain reorientation is affected according to the twin variant exhibiting the highest twin volume fraction, amongst the twin slip systems. To ensure that the newly instantiated child grain results in stable stress-strain updates, the following steps are followed based on the work of Abdolvand et al. [20]

1. The Cauchy stress in the parent grain and the child grain is set to be equal at twin inception.
2. The slip systems in the child grain are rotated using the rotation tensor specified in Eq. (10).
3. The CRSS of the slip systems in the child grain is set to be equal to that of the parent counterparts.
4. The resolved shear stress on the slip systems are re-computed using the Cauchy stress and the rotated Schmid tensors. If the resolved shear stress value is greater than the CRSS (due to the rotation), we set it to be equal to the CRSS value at that iteration.
5. All other twins are de-activated in the parent grain.

Note that the entire Gauss point may be filled with the child grain, after sufficient deformation. Changes to the state variables within the twinned portion of the grain are summarized in Table 1. The overall mechanical response of the composite parent-child system is given as the Taylor average of the

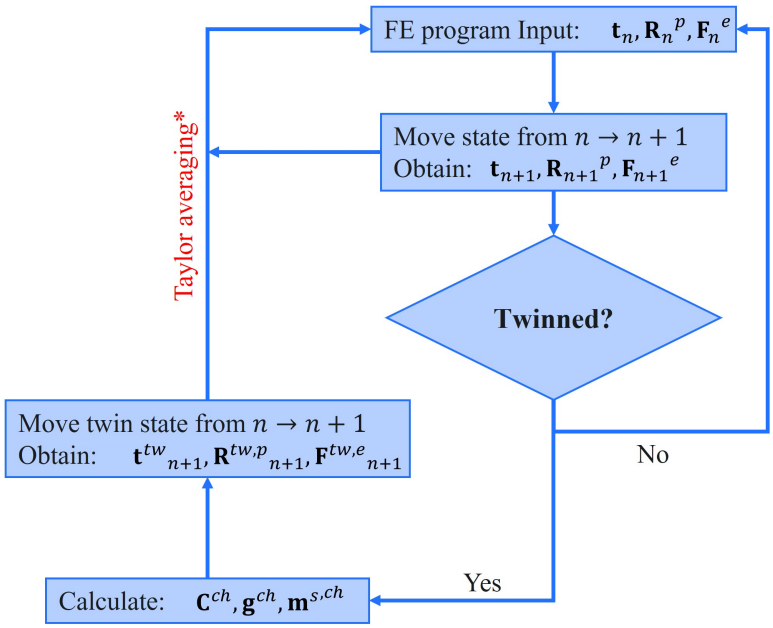

Figure 2: Workflow of incorporating twinning crystal plasticity formulation in FEM code WARP3D.

updated stresses in the child grain and parent grain, as follows:

$$\begin{aligned} \boldsymbol{\sigma}^{n+1} &= \boldsymbol{\sigma}^{n} + \Delta\boldsymbol{\sigma}, \\ \Delta\boldsymbol{\sigma} &= \left(1 - \sum_{\beta=1}^{N^{tw}} f^{\beta}\right) \Delta\boldsymbol{\sigma}^{pa} + \sum_{\beta=1}^{N^{tw}} f^{\beta} \Delta\boldsymbol{\sigma}^{ch} + \sum_{\beta=1}^{N^{tw}} \Delta f^{\beta} (\boldsymbol{\sigma}^{ch} - \boldsymbol{\sigma}^{pa}), \end{aligned} \tag{11}$$

where n is the iteration number, $\boldsymbol{\sigma}^{pa}$ is the stress in the parent grain, and $\boldsymbol{\sigma}^{ch}$ is the stress in the child grain.

The flowchart in Fig. 2 schematically represents the algorithmic workflow utilized in this study to accomplish this task. At each time increment, it is checked if the twin threshold is reached or not. If not, only slip calculations are performed and the stress state is updated. If the threshold is reached then, the child grain is reoriented and twining calculations are performed for the child grain. Slip calculations are performed for the remaining grain and the Taylor averaging method is used to obtain the overall stress state of the grain. The details about specific changes in the source code are explained in Appendix A.

4. Results and discussion

4.1. Single-crystal

A symmetric cubical geometry with each side of 1 mm was used to simulate the channel die compression test of a single crystal of Zircaloy. A schematic of the simulation is shown in Fig. 3, and

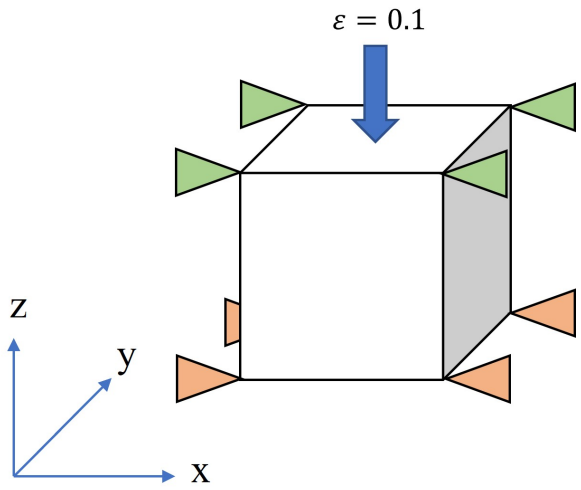

Figure 3: Setup of single crystal model with a single finite element to simulate the channel die compression test.

it replicates the setup utilized in the experimental study conducted by Kelly et al. [56] and Liang et al. [57]. The geometry was meshed with a single brick element with 8 nodes for simplicity. Green triangles represent the nodes that are constrained to move in x direction only whereas orange triangles represent the nodes that are restricted to move in x as well as z direction. The compressive strain of value 0.1 was applied on the top surface of the element as shown in Fig. 3. The strain was applied with the help of displacement boundary condition in the form of a total of 4000 increments.

Simulations were performed for various loading and constraint directions which are illustrated in Fig. 4. The Blue arrow indicates the direction of loading and the orange plane represents the constraint. The loading and constraint directions are always parallel to the sample z and x directions, respectively. These configurations are designed to activate specific families of slip systems preferentially over others, which would in turn aid in isolating their effects on the overall mechanical response. For instance, the loading along the c-axis of the HCP single crystal in case 1 preferentially activates the pyramidal $< c + a >$ systems whereas case 5 preferentially activates the basal systems due to the maximization of the Schmid factor. However, it should be pointed out that in a rate-dependent framework, typically all slip systems exhibit non-negligible slip activity. We denote active slip systems as those slip systems wherein the accumulated slip exceeds 5% of the total accumulated slip across all slip systems. The elastic and plastic material constants for the Zircaloy were obtained from Fischer and Renken [58], and Abdolvand et al. [20], respectively.

Fig. 5 shows the stress-strain response of a single crystal of Zircaloy under compressive loading in five different orientations. Fig. 5(a) shows the response with implemented twinning model hence with three slip systems along with one additional twin system and Fig. 5(b) without implementing

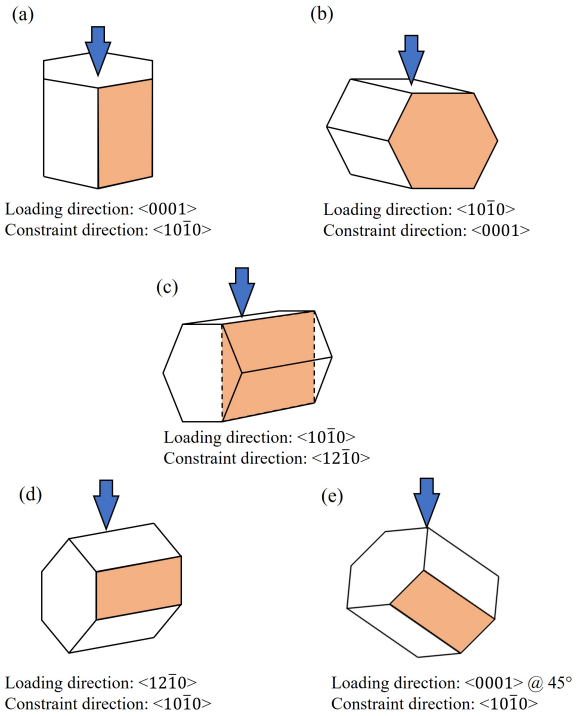

Figure 4: Crystal orientations used in the single crystal channel die compression tests.

twinning model hence with only three slip systems. It can be seen that twinning plays an important role in the response of Zircaloy single crystal in some orientations. Activation of the twin system can be observed as a kink in a stress-strain curve for cases 2 and 3. To further understand the role of twinning in different loading orientations, slip and twin activities during the compression are shown in Fig. 6 to Fig. 10. Here activity is quantified using the value of accumulated plastic strain on the particular slip or twin system. It shows that the different deformation mechanisms get activated in different load cases. For instance, case 1 is the only case where the Pyramidal <c+a> systems show any degree of noticeable slip activity since the loading direction is aligned along with the c-axis initially. Even in this case, the onset of twinning immediately activates basal slip in the twinned portion of the grain. Further evolution of the twinning volume fraction brings an increasing portion of the grain in alignment with a direction that is close to perpendicular to the loading direction ($\Phi = 90^o$), allowing the activation of the prismatic systems as well.

Case 2 represents a crystal that is well-aligned for singular prismatic slip, but since this would violate compatibility (i.e. 5 independent slip systems must be active to accommodate an arbitrary external plastic stretching tensor), the twinning volume fraction also evolves rapidly along with the prismatic slip activity. The twinning of the grain in case 2 aligns the twinned portion of the grain for basal slip, whose effects are clearly visible in Fig. 7. The necessity of maintaining plastic compatibility

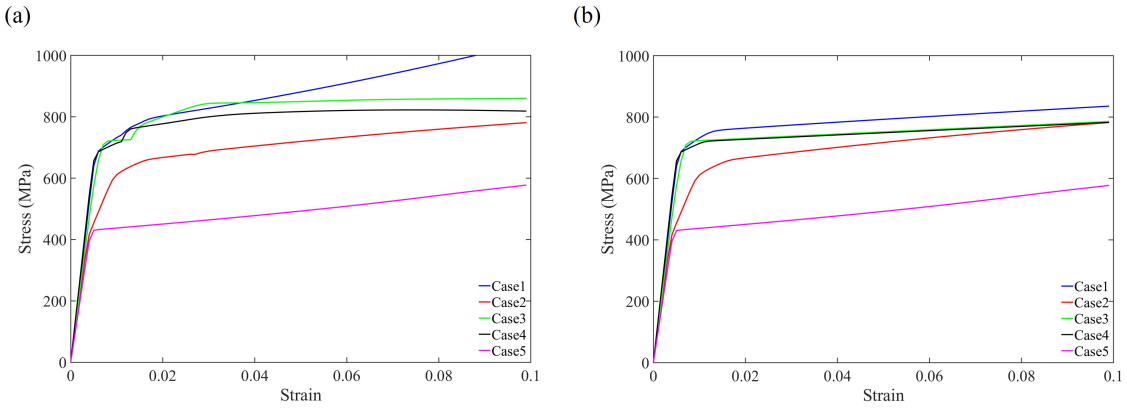

Figure 5: Stress-strain curves obtained from single crystal channel die compression tests of Zircaloy with (a) twinning model ON, and (b) twinning model OFF.

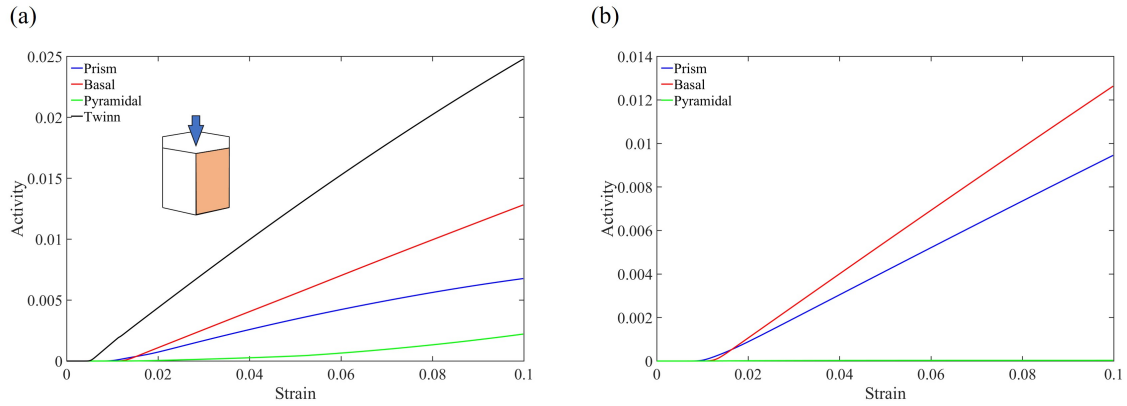

Figure 6: Slip and twin modes activity during compression test of Zircaloy single crystal loaded in case 1 orientation (a) with and (b) without considering twinning deformation.

results in a rapid reduction in the volume fraction of the parent grain, which in turn causes a rapid increase in basal slip activity. This relative increase in the basal slip activity manifests as a lower value in the stress in the loading direction, since the basal CRSS is the lowest amongst the slip families.

Cases 3 and 4 exhibit a high degree of twinning activity, and twinning induced reorientation form a major component of the deformation mechanism (especially case 3). The reorientation results in a saturation of the stress-strain response in the middle ranges of strain, followed by a sharp spike that reflects the activation of other slip families. From Figs. 8 and 9, it is clear that the prismatic systems exhibit higher rates in case 3 as compared to case 4. In addition, the twinning induced reorientation proceeds far more rapidly in case 4 as compared to case 3, and it results in a large portion of the crystal being well aligned for basal slip. Therefore, it is clear why case 3 exhibits a relatively higher stress response as compared to case 4.

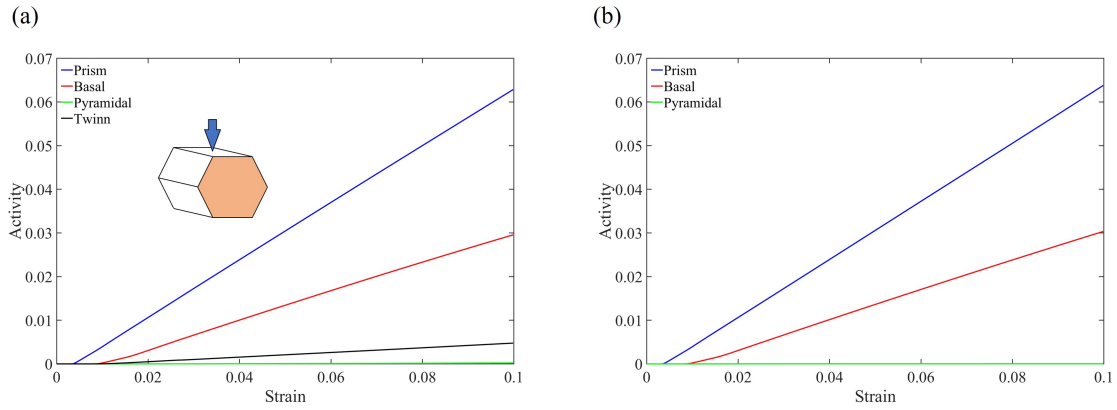

Figure 7: Slip and twin modes activity during compression test of Zircaloy single crystal loaded in case 2 orientation (a) with and (b) without considering twinning deformation.

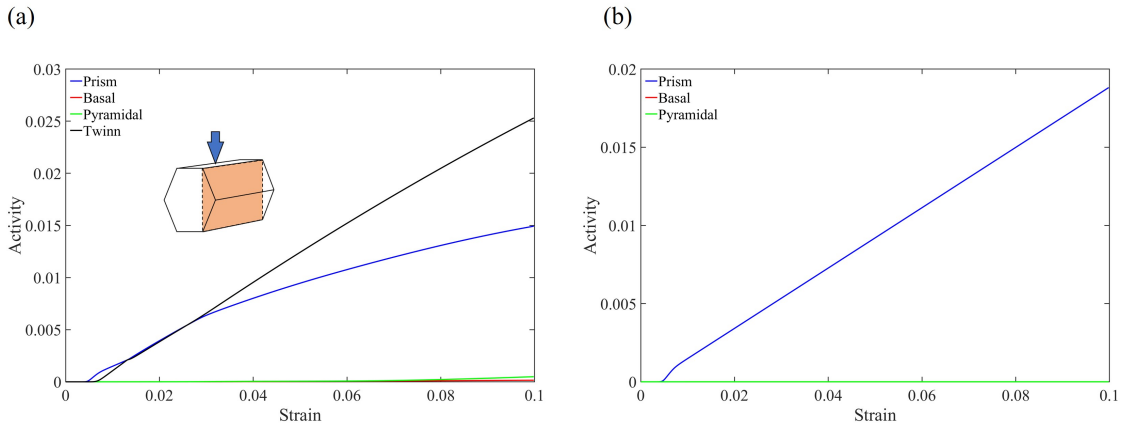

Figure 8: Slip and twin modes activity during compression test of Zircaloy single crystal loaded in case 3 orientation (a) with and (b) without considering twinning deformation.

Case 5 represents a crystal that is well aligned for basal $< a >$ slip. Since the CRSS of the basal systems is much lower than the Pyramidal $< c + a >$ systems, they exhibit negligible slip activity in comparison to them. It should be pointed out that prismatic and twinning systems are largely inactive due to very low Schmid factors. The predominance of basal slip and the low amount of slip in the Pyramidal $< c + a >$ systems results in this case exhibiting the lowest stress response out of all the cases.

4.2. Poly-crystal

A cubical RVE of dimensions $1 \times 1 \times 1$ mm^3 was created to simulate a uniaxial tensile test for polycrystal Zircaloy. The RVE contained 1000 hexagonal elements which is shown in Fig. 11(a) along with boundary conditions to mimic the uniaxial tension test. Symmetry boundary condition was

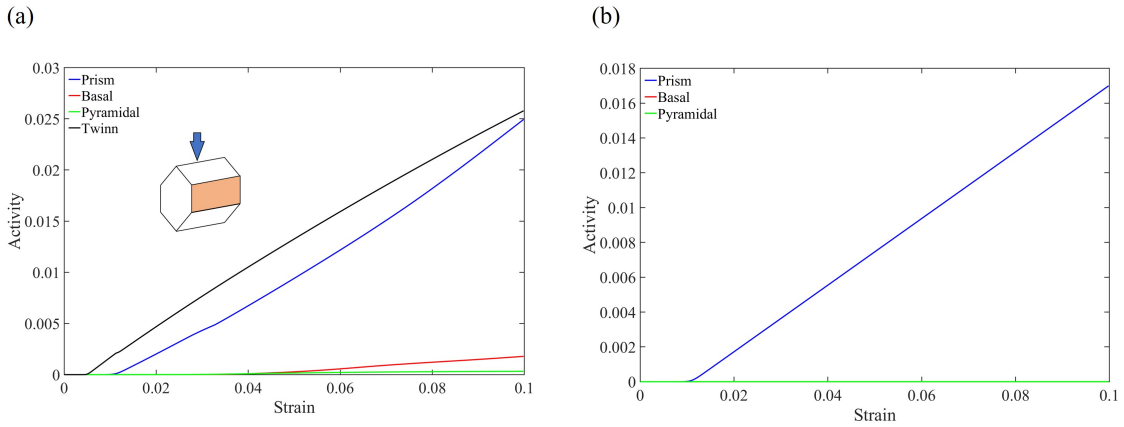

Figure 9: Slip and twin modes activity during compression test of Zircaloy single crystal loaded in case 4 orientation (a) with and (b) without considering twinning deformation.

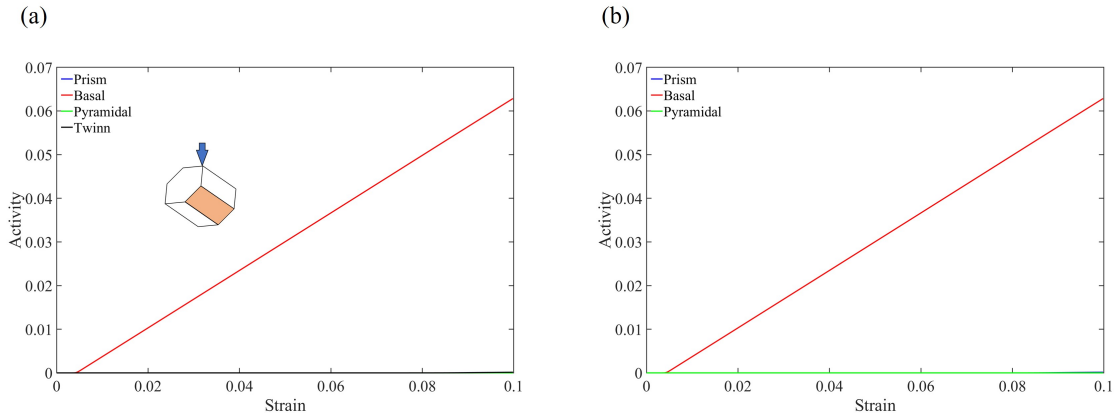

Figure 10: Slip and twin modes activity during compression test of Zircaloy single crystal loaded in case 5 orientation (a) with and (b) without considering twinning deformation.

applied on three faces of RVE which can be denoted by planes $x = 0$, $y = 0$, and $z = 0$. A uniform displacement boundary condition of 0.05 mm was applied on the face $x = 1.0$ in a total of 5000 equal increments. All the nodes on the face $y = 1.0$ are constrained to have the same displacement in y direction, and all the nodes on the face $z = 1.0$ are constrained to have the same displacement in z direction. These constraints are applied to avoid any warping of RVE surfaces, and they approximate the zero transverse traction boundary conditions of a uniaxial tension test and have been employed in other CPFEM studies using Neper [59]. While not as high-fidelity as periodic boundary conditions, these constraints do improve upon fully fixed conditions for which the RVE's external grains are typically suppressed from post-processed statistics [60]. Xu et al. [61] utilized the Neutron Diffraction technique to measure the texture of the mid-section of a warm-rolled Zircalloy plate and noted a strong basal texture. The measured texture was input as a text file into the synthetic microstructure

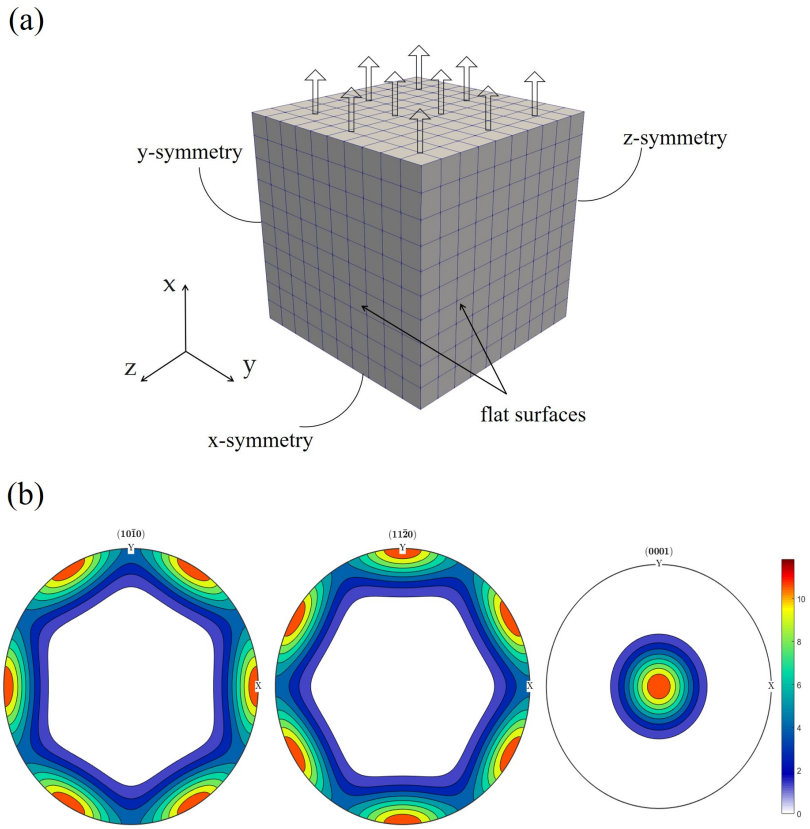

Figure 11: (a) Setup of a polycrystal model with 1,000 individual grains, and (b) strong basal structure assigned to the grains.

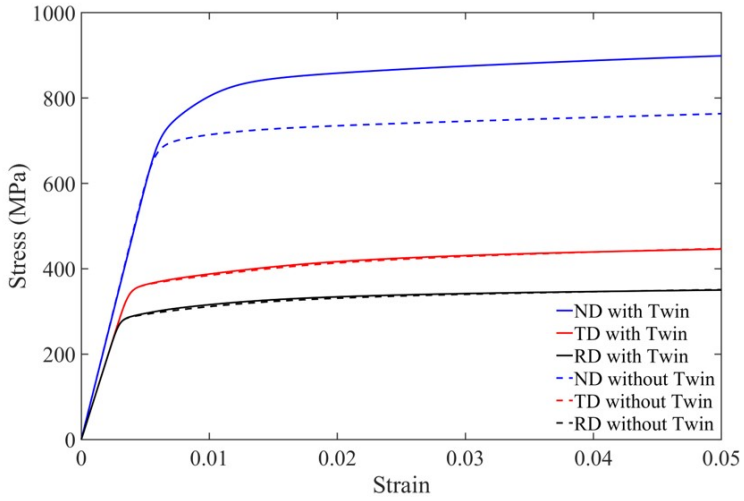

Figure 12: Stress-strain response of Zircaloy for different loading directions with vs without twinning model.

generation software DREAM-3D developed by Groeber et al. [62]. DREAM-3D packs ellipsoids in the RVE by using the supplied grain size statistics, following which the grain orientations are randomly generated and assigned in order to match the supplied texture. Since exact grain size statistics were not available from the neutron diffraction experiments, we utilize an ensemble average to estimate the mechanical response along the loading direction. Every element in RVE represents a separate grain and a strong basal grain orientation was assigned as shown in Fig. 11(b).

We note that the presence of a strong basal texture in the underlying sample results in a highly anisotropic mechanical response in the TD (in an RD-TD-ND convention) direction as compared to the RD and ND directions, as shown in fig. 12. This is due to the high density of grains with the c-axis parallel to the loading direction, which results in tensile twinning and pyramidal <c+a> slip being the dominant modes of deformation. The dashed lines in Fig. 12 show the response of Zircaloy RVE without considering the deformation due to twin. The tensile twin gets activated in ND case resulting in huge difference in stress values along ND case but the RD and ND results predominantly reflect the activation of the prismatic and basal slip, and very little, if any tensile twinning is observed in these cases. The difference between the RD and ND cases is due to the directional differences in the densities of 0002 planes w.r.t each other. The exact values of the initial CRSS for the different slip families control the initial yield in the different directions, whereas the values g_1^α control the saturation values of the yield curve. The hardening parameters θ_0^α and θ_1^α control the slope of the hardening curve w.r.t the strain axis.

5. Sensitivity analysis

One of the main challenges of performing CPFEM simulations using any material is the difficulty in obtaining material parameters. For multiple CP models, the parameters can not be obtained experimentally due to the complexity of creating a single crystal specimen. Also, a large number of material parameters (for the model studied in this paper 22) make it difficult to find a unique set of parameters. There is a possibility to have multiple sets of parameters resulting in the same stress-strain curve of the uniaxial tension test. And lastly, the anisotropy in the material response requires performing calibration of at least three stress-strain curves simultaneously. Therefore, a sensitivity analysis was conducted to understand how each parameter in the CP model affects the material response. As the material response is also highly dependent on loading direction, five different loading directions were considered for the single crystal model and three different directions for the polycrystal model. Elastic parameters were not varied and only plastic parameters were varied in a certain range.

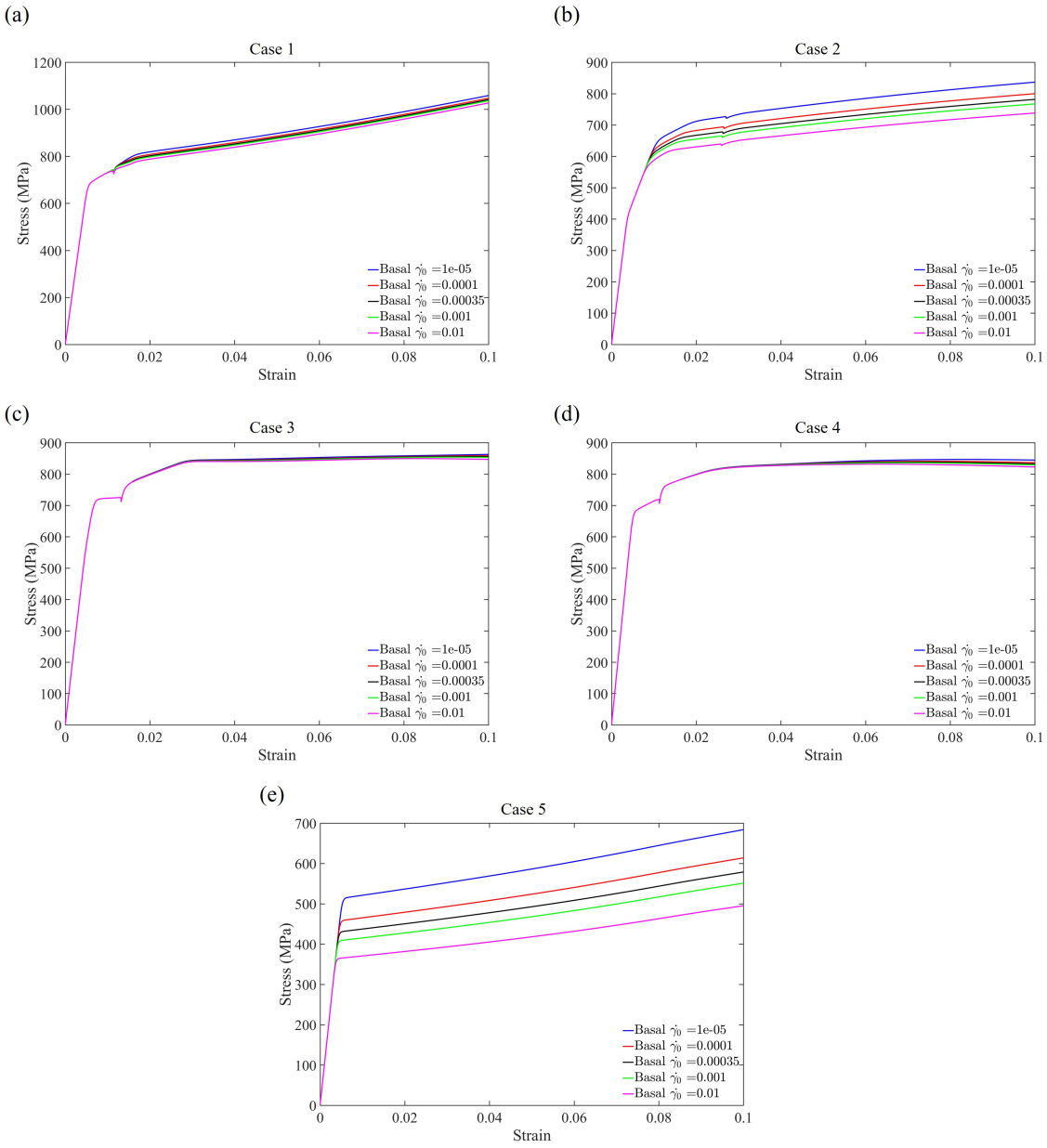

Figure 13: Stress-strain response of single crystal of Zircaloy for different values of CP material model parameter basal $\dot{\gamma}_0$ for five different loading orientations.

5.1. Single-crystal

A cubical RVE meshed with a single brick element was loaded under uniaxial tension to obtain its mechanical response. Symmetric boundary conditions were applied as discussed in section 4.1 while considering the same five orientations shown in Fig. 4. Fig. 13 shows the stress-strain curves for five loading cases for five different values of parameter basal $\dot{\gamma}_0$. Twin mode was activated in all the loading

cases except case 5. As seen in Fig. 13(a), the parameter basal $\dot{\gamma}_0$ did not have any effect on the yield stress value of the crystal in case 1 loading. The activation of the twin can be observed as a kink and only after this point the effect of the change of parameter value can be seen. The slope of hardening of the material remained the same but the stress value at 10 % strain was affected due to a change in the parameter value. As the value of basal $\dot{\gamma}_0$ increased from 1×10^{-5} to 0.01 /s, the value of stress at 10 % strain decreased. In case 2 shown in Fig. 13(b), the yield stress again remained unaffected by the change in the parameter value. Contradictory to case 1, in case 2 the effect of change in the value of the parameter affected the stress-strain curve before activation of twin mode. Again a little effect can be found on the hardening slope but a larger effect was seen on the stress value at the 10 % strain.

Stress strain plots obtained in cases 3 and 4 had a similar effect due to variation of basal $\dot{\gamma}_0$ parameter. Yield and hardening slope remained unaffected with a small variation in the stress value at 10 % strain. Case 5 had the most effect of variation in the basal $\dot{\gamma}_0$ parameter as shown in Fig. 13(e). The tensile twin was not activated in this case resulting in the smooth stress strain curve. In this case 5, the parameter value had a huge impact on the yield stress. An increase in the parameter value caused a decrease in yield stress, hardening slope, and stress value at the 10 % strain.

Fig. 14 shows another way to represent the results shown in Fig. 13. Here, three quantities of interest are chosen which are yield stress, hardening slope, and stress at 10 % strain. The variation of each of these quantities with respect to the material parameter basal $\dot{\gamma}_0$ is shown in Fig. 14. Interpreting the results in Fig. 14 is considerably simpler than the results in Fig. 13 showing the stress strain curves. For example, Fig. 14(a) shows that the variation in basal $\dot{\gamma}_0$ parameter does on affect the yield stress value for the crystal loaded in case 1 to case 4. It affects the yield stress value only in case 5 where an increase in the material parameter causes a decrease in the yield stress. Fig. 14(b) shows that the hardening slope has a little effect of variation in the basal $\dot{\gamma}_0$ parameter. Fig. 14(c) shows that cases 2 and 5 have a larger effect compared to cases 1, 3, and 4 on the stress value at the 10 % strain due to change in basal $\dot{\gamma}_0$ parameter. Similarly plotting and discussing the results of all 22 material parameters on five different loading cases would make this paper too lengthy and tedious. Therefore, the same results for all the 22 parameters can be presented in more simplified way related to yield stress in Figs. 15 and 16 and related to stress at 10% strain in Figs. 17 and 18.

Fig. 15 shows the effect of variation in the parameters 1 to 16 on the yield stress of single crystal of Zircaloy for five different loading directions. Increase in the yield stress while material parameter increases results in positive value of bar plot and decrease in the yield stress while material parameter increases results in negative value of bar plot. All the bar values are normalized based on maximum change in yield stress being equal to 100 %. Similar results for parameter 17 to 22 are shown in Fig. 16. Parameters 21 and 22 are kept separate due to their separate role in the constitutive model. The twinning model parameters were found to have a significant impact on the yield stress in cases 1,

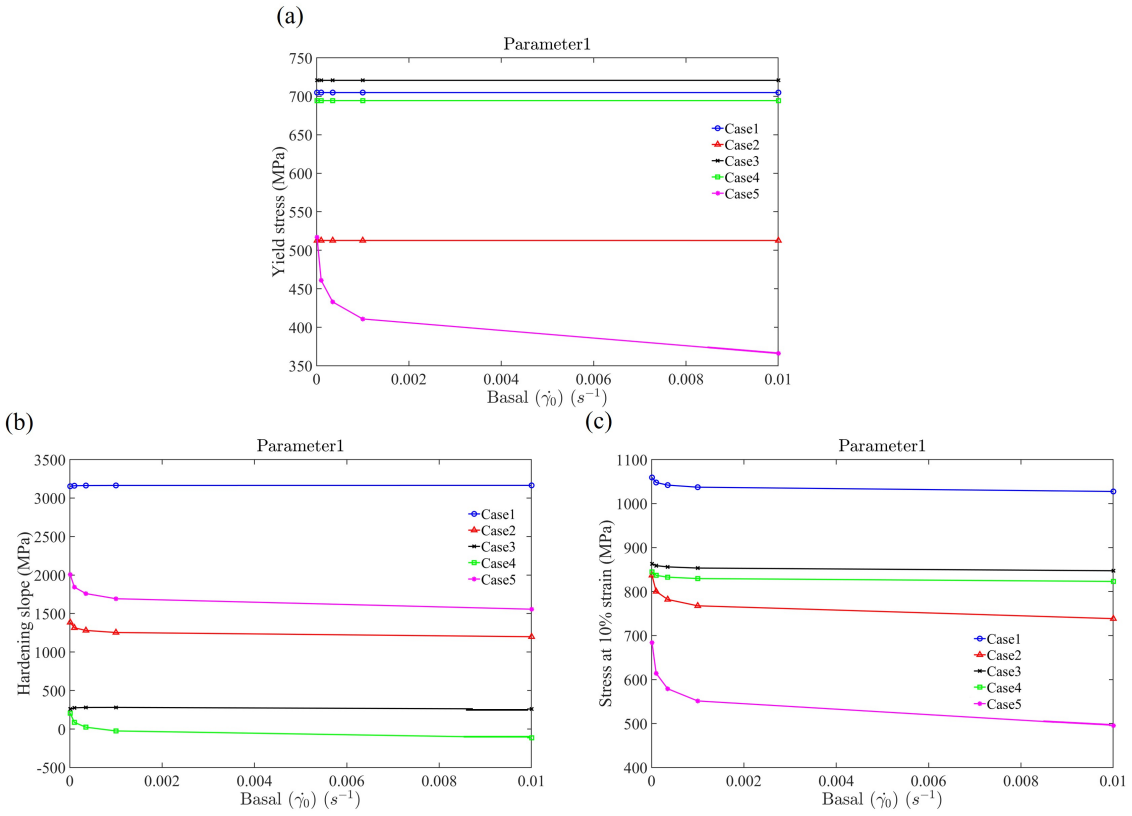

Figure 14: Variation of (a) yield stress, (b) hardening slope, and (c) stress at 10 % strain with respect to the value of CP material model parameter Basal $\dot{\gamma}_0$ for five different loading cases.

3, and 4 with negligible impact on case 2 and 5. All basal material parameters had impact only in case 5 which shows the strong basal influence along that direction. Prismatic parameters mostly influenced case 2 with pyramidal parameters had minimum impact on all directions. Parameter m was found to be the only parameter to effect the yield stress in all five cases. Parameter γ_{tw} was found to have no effect on the yield stress of single crystal of Zircaloy in any loading orientation.

Figures 17 and 18 shows the effect of variation in the parameters 1 to 22 on the stress value at 10 % strain of single crystal of Zircaloy for five different loading directions. Overall, the twinning parameters were found to have a large effect on the stress value at 10% strain followed by prismatic and pyramidal parameters. Some unique behavior was observed where increase in the value of the parameter caused stress value at 10 % strain to increase in some cases and decrease in other cases. This behavior was found with respect to parameters pyramidal $\dot{\gamma}_0$, pyramidal g_1, prismatic θ_1, and γ_{tw}. Similar bar plots can be given for hardening slope but are not given in this paper for brevity. These results can be used for the calibration of any HCP material using the same CP model as described in section 2.

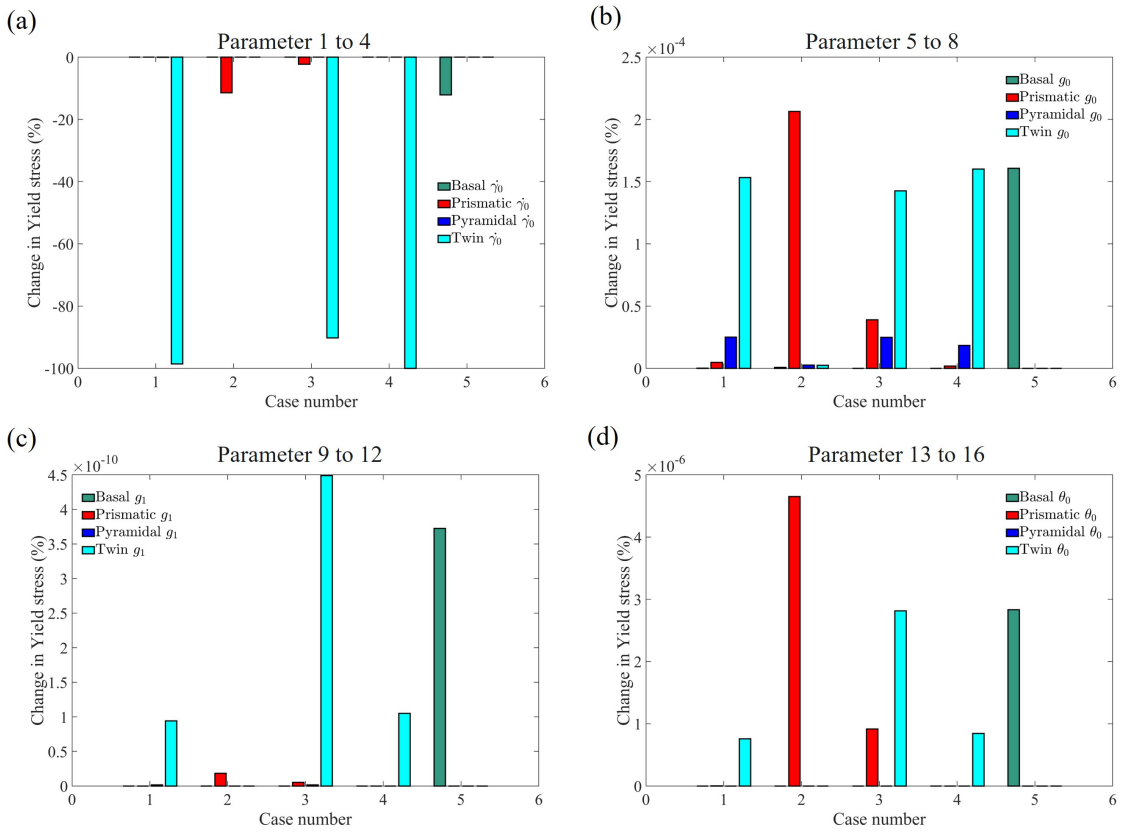

Figure 15: Sensitivity analysis results showing the effect of parameters 1 to 16 on the yield stress of a single crystal of Zircaloy.

5.2. Poly-crystal

Most of the components made from Zircaloy are polycrystalline materials as it is challenging to grow a single crystal with large dimensions. Hence it is important to understand the effect of different parameters on the stress strain curve of polycrystalline material. Same polycrystalline RVE of Zircaloy under uniaxial tension loading was considered for sensitivity analysis as shown in Fig. 11(a) along with boundary conditions. Fig. 19 shows the stress-strain response of polycrystal RVE of Zircaloy for different values of CP material model parameter basal $\dot{\gamma}_0$ for loading in (a) ND, (b) RD, and (c) TD case. The parameter value was varied between 10×10^{-5} to 0.01 while keeping all the parameters constant. Twinning mode activation was smoother compared to single crystal material due to averaging of a large number of grains. As the value of parameter basal $\dot{\gamma}_0$ increased the value of yield stress decreased in ND loading case. Yield stress did not change in the case of RD and TD case due to variations in basal $\dot{\gamma}_0$ parameter but the slope of hardening was affected which also results in change of stress value at 5% strain.

For simplification and ease of understanding, all the results were converted to bar charts as described

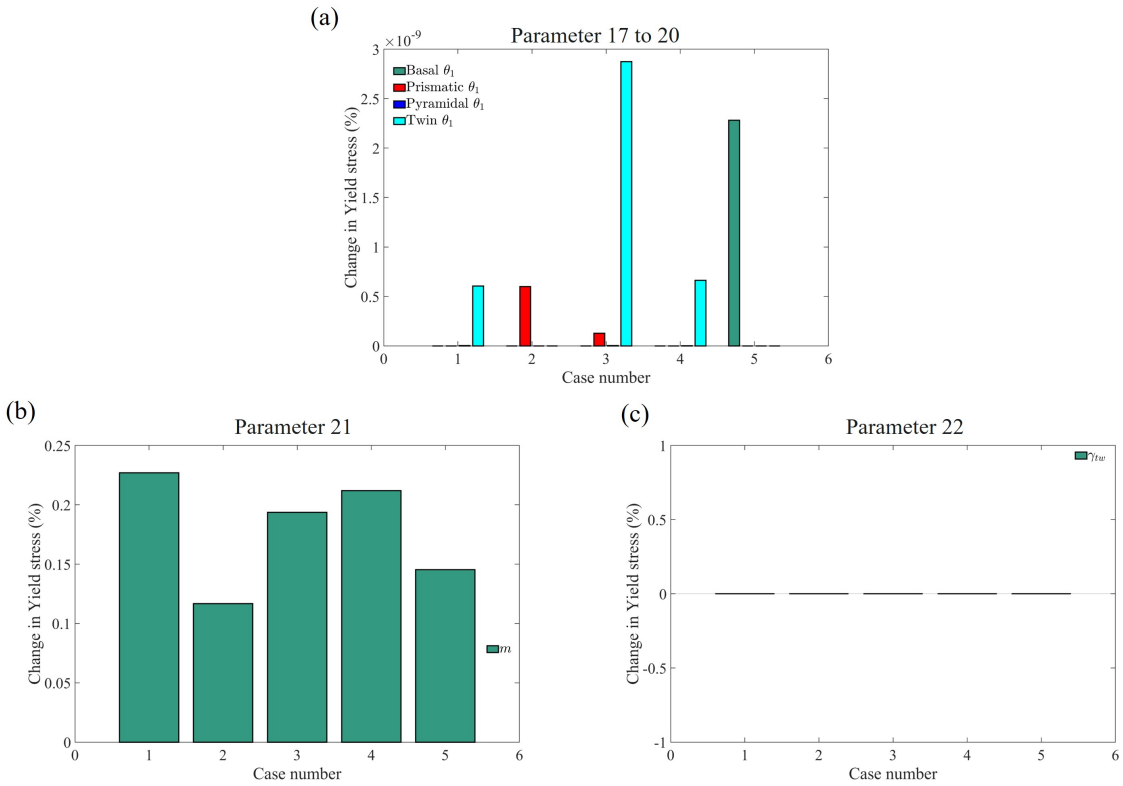

Figure 16: Sensitivity analysis results showing the effect of parameters 17 to 22 on the yield stress of a single crystal of Zircaloy.

in an earlier subsection. Figures 20 and 21 shows the effect of variation in the parameter 1 to 22 on the yield stress of polycrystal of Zircaloy for three different loading directions. Twin $\dot{\gamma}_0$ was found to have the highest effect on the yield stress of the polycrystal RVE. The twin g_0 parameter affects the yield stress of only ND loading. Prismatic γ_0, g_0 , and g_1 parameters alter the yield stress of TD and RD cases equally without changing the yield stress of ND loading. Pyramidal g_1 and θ_1, basal g_1, and twin g_1 are some of the parameters which simultaneously increase and decrease the yield stress in different cases.

Figures 22 and 23 shows the effect of variation in the parameters 1 to 22 on the stress value at 5 % strain of polycrystal of Zircaloy for three different loading directions. Twin $\dot{\gamma}_0$ parameter was again found to have the highest effect on the stress at 5% strain of the polycrystal Zircaloy RVE with increase in the parameter value causing the decrease in the stress value. Increase in the pyramidal g_1 parameter increases the stress value in all three cases whereas prismatic g_0 and θ_0 increases the stress in TD and RD cases significantly more than ND case. Parameters such as prismatic g_1 and twin g_1 did not have any effect on stress value in any direction.

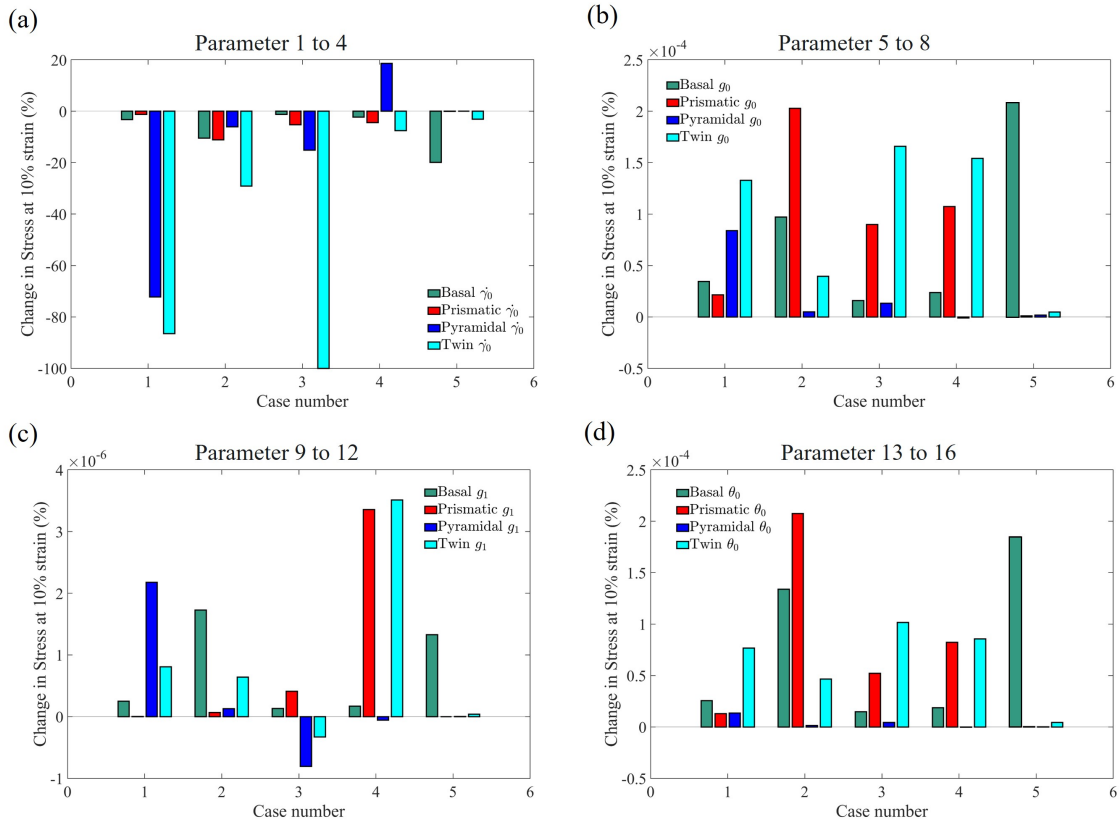

Figure 17: Sensitivity analysis results showing the effect of parameters 1 to 16 on the stress value at 10 % strain of a single crystal of Zircaloy.

5.3. Calibration of material parameters

Xu et al. [63] performed uniaxial tensile testing on a polycrystal Zircaloy-2 sample with composition as Zr with 1.43 – 1.45 wt.% Sn, 0.13 – 0.14 wt.% Fe, 0.1 wt.% Cr, 0.05 wt.% Ni, 1260 – 1440 wt. ppm O, and 150 – 160 wt. ppm C. Experimental pole figures showed a strong basal orientation along the normal direction (ND). They performed tensile tests along three directions (ND, TD, and RD) and reported the stress-strain curves that are shown in Fig. 24. The recorded stress-strain response under tension along ND was also about 25% stronger compared to tension along RD and TD. A well-calibrated CP model should be able to predict all three stress strain curves with only one set of material parameters where anisotropic behavior comes from the CP model itself. Elastic constants for this Zircaloy-2 material are well established in the literature [58, 20]. An initial guess was made for all the CP material parameters and corresponding stress strain curves for all the loading directions are shown in Fig. 24(a). It is seen that the slope of the stress strain curve in each case is very well reproduced in the elastic region. Suggesting that the elastic constants used in the modeling are quite reasonable and that the texture has been well represented. But, the correlation along the ND direction

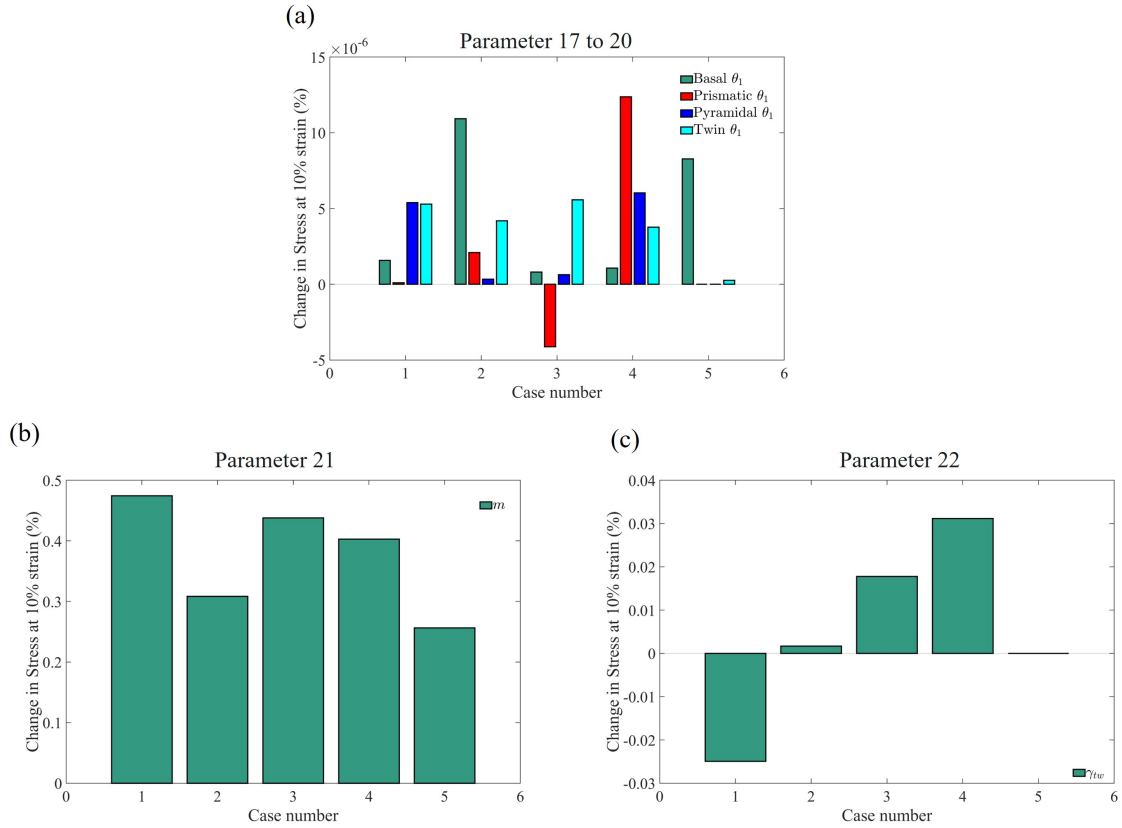

Figure 18: Sensitivity analysis results showing the effect of parameters 17 to 22 on the stress value at 10 % strain of a single crystal of Zircaloy.

is way off and the response along the TD and RD loading is almost the same which is not the case in the experimental curves.

Due to the complex nature of the CP model and a large number of material parameters, it is almost impossible to simultaneously fit all three curves by using the trial and error method. One way would be the use of an optimization algorithm or machine learning (ML) model trained using a sensitivity analysis conducted in this work but it is out of the scope of this manuscript. We used the results of sensitivity analysis shown in figures 20 to 23 to manually adjust the CP parameters. After a couple of iterations, a good fit was observed between experimental and simulation results as shown in Fig. 24(b). The final CP material parameters are given in Table 2.

6. A case study: Effect of hydride volume fraction

Zircaloy, an alloy of mainly zirconium and tin, is a common cladding material in nuclear applications where its main purpose is to provide structural integrity [64, 65, 66, 67]. In addition, in some applications Zircaloy is also used as a getter to collect the tritium; an isotope of hydrogen. This is

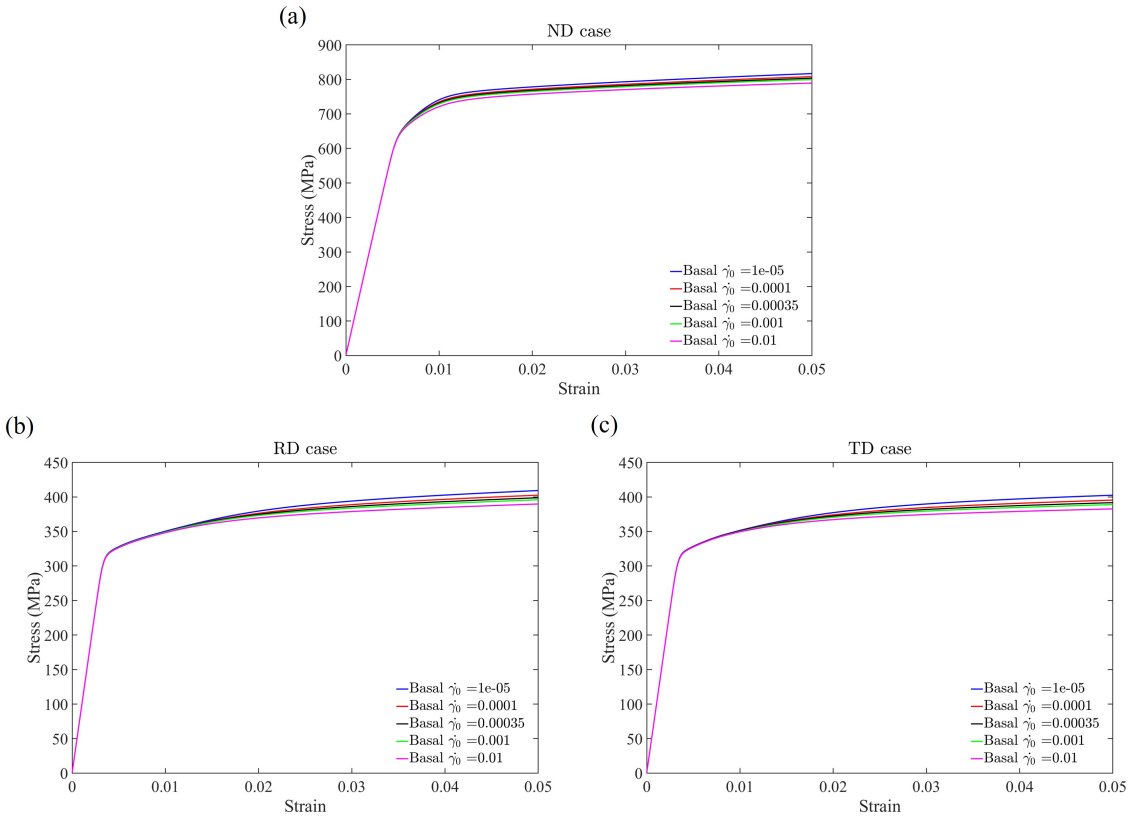

Figure 19: Stress-strain response of polycrystal of Zircaloy for different values of CP material model parameter basal $\dot{\gamma}_0$ for loading in (a) ND, (b) RD, and (c) TD case.

Table 2: Calibrated CP material parameters for Zircaloy-2.

System	**Parameter**	**Value**	**System**	**Parameter**	**Value**
Basal	$\dot{\gamma_0}$	3.5×10^{-4}	Pyramidal	$\dot{\gamma_0}$	1.0×10^{-2}
	g_0	168.0		g_0	331.0
	g_1	220.0		g_1	270.0
	θ_0	50.0		θ_0	100.0
	θ_1	0.0		θ_1	280.0
Prismatic	$\dot{\gamma_0}$	3.5×10^{-4}	Twin	$\dot{\gamma_0}$	1.0×10^{-4}
	g_0	120.0		g_0	100.0
	g_1	330.0		g_1	200.0
	θ_0	50.0		θ_0	20.0
	θ_1	200.0		θ_1	0.0
	m	0.05		γ_{tw}	0.629

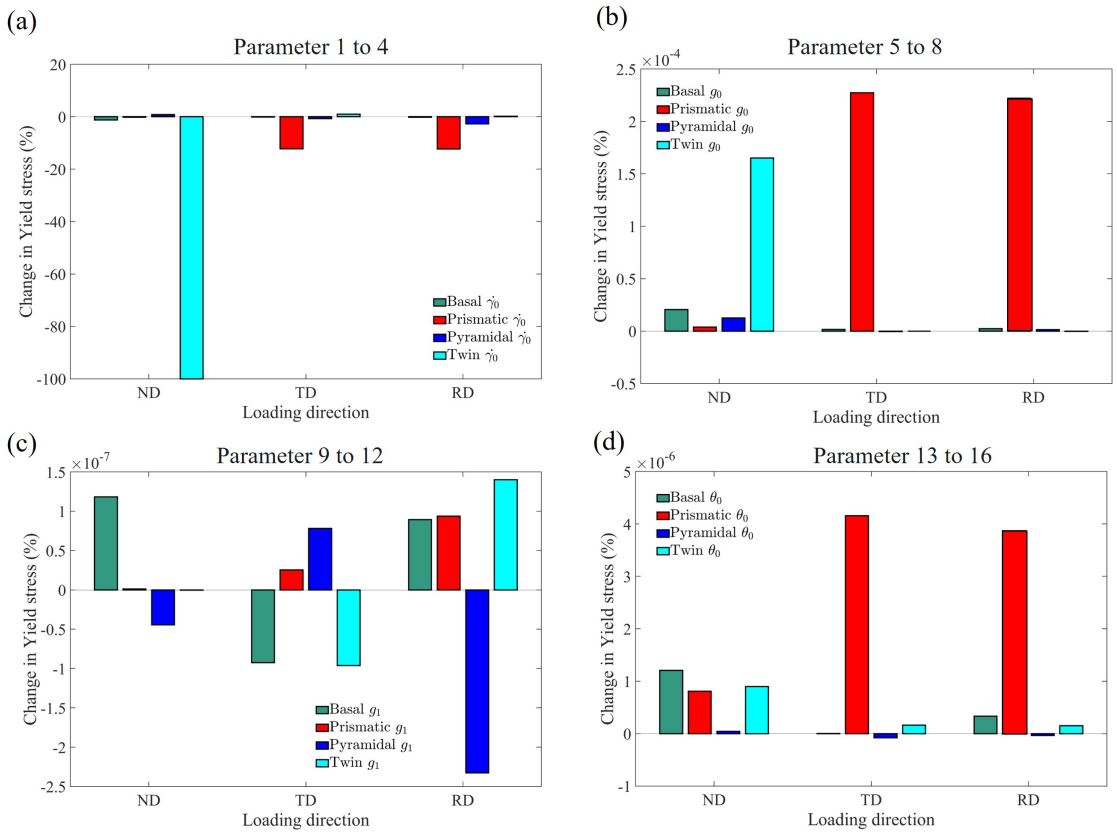

Figure 20: Sensitivity analysis results showing the effect of parameters 1 to 16 on the yield stress of a polycrystal RVE of Zircaloy.

achieved by encapsulating the lithium pellets by Zircaloy getter in tritium producing burnable asborber rod (TPBAR). During TPBAR's operation, it was observed that the free hydrogen diffuses through Zircaloy and forms clusters of zirconium hydrides [68]. As the formation of the hydride phase alters the mechanical properties of Zircaloy, it is important to determine the new altered mechanical properties of the heterogeneous material. The parameter 'volume fraction' can be used to quantify the measure of the zirconium hydride phase in the Zircaloy matrix. The hydride volume fraction can be defined as the ratio of the volume of the hydride phase to the volume of the whole RVE. Since the overall properties of RVE will change, if the hydride volume fraction changes, we created multiple RVEs with increasing volume fraction from 0.05 to 0.3 as shown in Fig. 25. The red-colored phase represents the Zircaloy and the gray-colored phase represents the zirconium hydride. The hydride phase is randomly dispersed into the Zircaloy matrix. The hydride was assumed to be isotropic elasto-plastic material with a value of Young's modulus as 110 GPa, Poisson's ratio as 0.32, and initial yield stress value being 400 MPa [44, 69]. Complete plastic material properties of hydride can be found in [44]. The RVE was loaded in uni axial tension load with the boundary conditions shown in Fig. 11(a). Again the strong

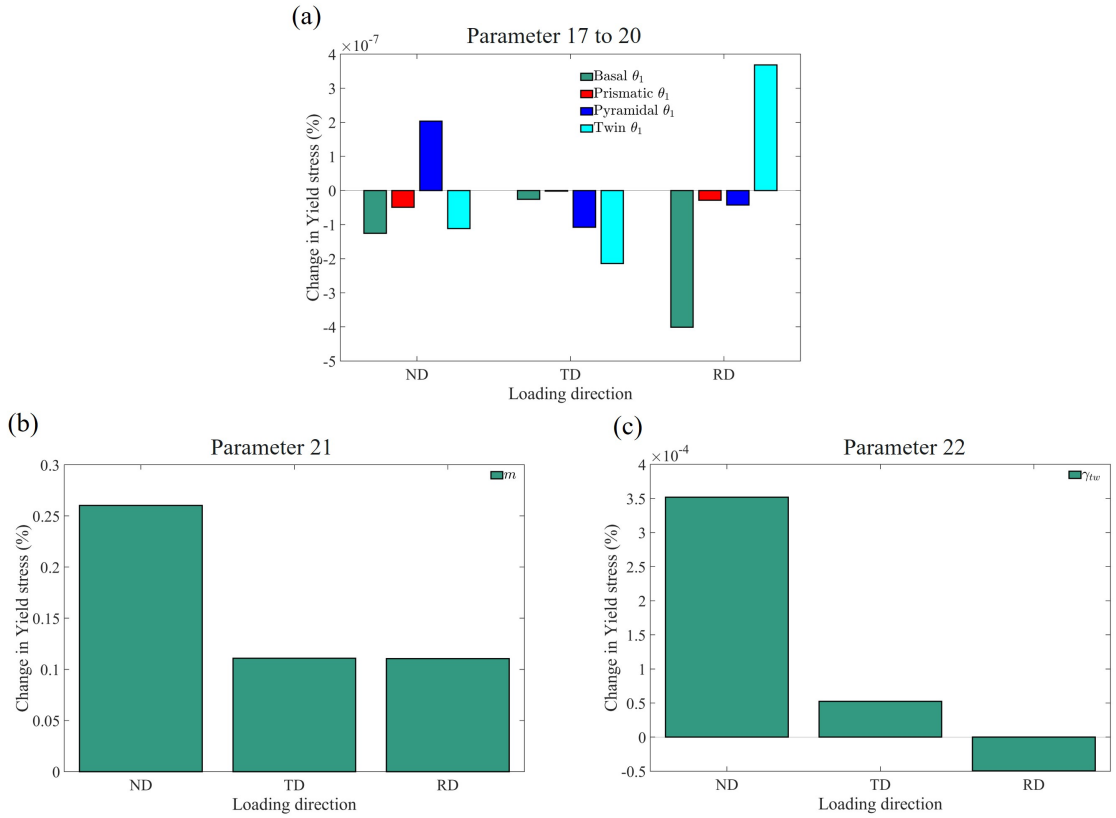

Figure 21: Sensitivity analysis results showing the effect of parameters 17 to 22 on the yield stress of a polycrystal RVE of Zircaloy.

basal structure was assigned to Zircaloy grains as shown in Fig. 11(b).

Fig. 26 shows the stress-strain response of Zircaloy RVE along (a) ND, (b) TD, and (c) RD loading for the different volume fractions of zirconium hydride. All the results are average of five different RVEs with the same volume fraction of hydride. This is done to reduce the effect of randomness of dispersed hydride phase on the overall results. It was observed that hydride volume fraction has a significant effect on the overall mechanical response of Zircaloy. Fig. 27 shows the effect of hydride volume fraction on (a) Young's modulus, (b) yield stress, (c) hardening slope, and (d) stress at 5% strain of RVE. As the hydride volume fraction increases, Young's modulus of the material also increases along all three loading directions as seen in Fig. 27(a). The relation is almost linear with an increase in the value of Young's modulus by 1 GPa for an increase in the hydride volume fraction by 0.05. Young's modulus along ND is always around 25% higher than TD and RD. The yield stress was also found to increase almost linearly with hydride volume fraction as shown in Fig. 27(b). The increase in hydride volume fraction of 0.05 roughly corresponded to the 5% increase in the yield stress value along all three directions. This trend is in good agreement with the experimental studies reported in the

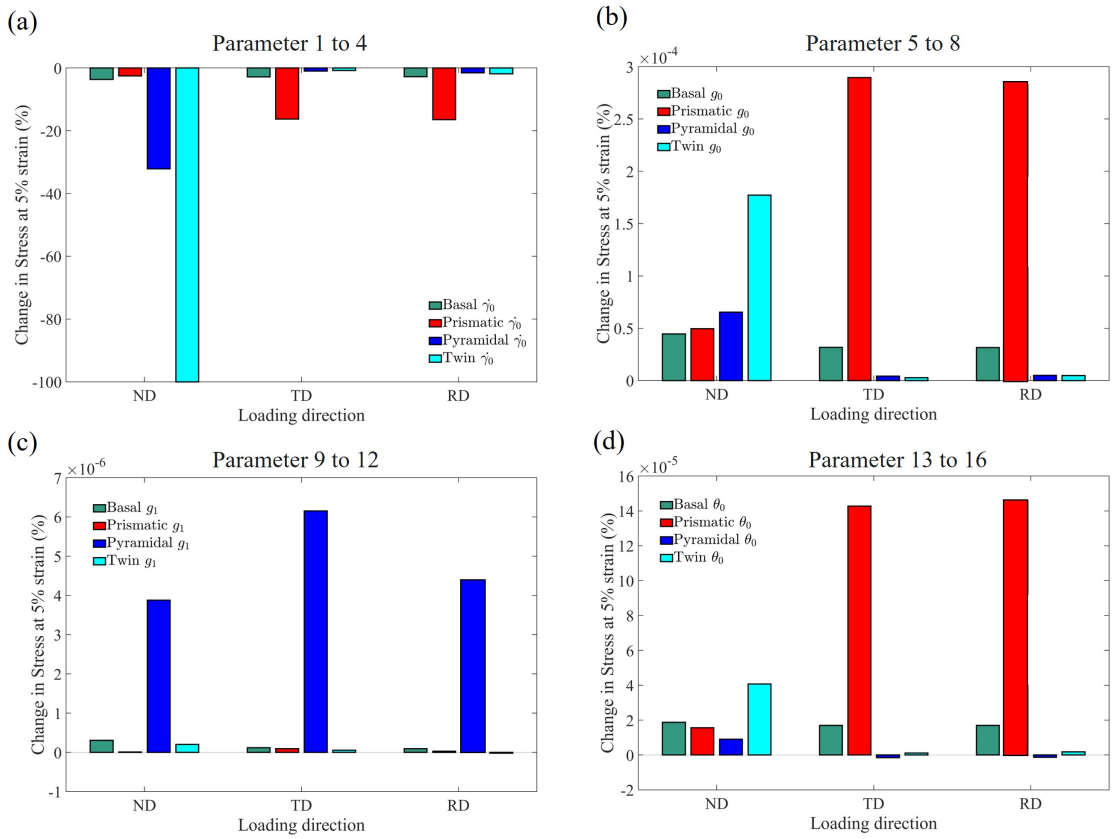

Figure 22: Sensitivity analysis results showing the effect of parameters 1 to 16 on the stress value at 5 % strain of a polycrystal of Zircaloy.

past [70, 71]. A similar trend was observed for both the hardening slope as well as stress value at the 5% strain as shown in figures 27(c) and 27(d). An increase hydride volume fraction by 0.05 roughly caused 15 % increase in the stress value at 5 % strain. A more detailed analysis of this phenomenon where hydride distribution was obtained via SEM images of actual microstructure can be found in our separate article [44].

7. Conclusion

Deformation due to slip and twin are two types of permanent deformations any crystallographic material such as metals and metal alloys can undergo. A crystal plasticity constitutive model can consider both of these deformation types while predicting the mechanical response of the material. In this work, a crystallographic twinning with the PTR scheme was implemented in a crystal plasticity module of the non-linear finite element code WARP3D. The slip system strength evolution model of extended Voce hardening law was also updated to incorporate the hardening law observed in Zircaloy. The implemented algorithm uses twin volume fraction to instantiate a new child grain within the parent

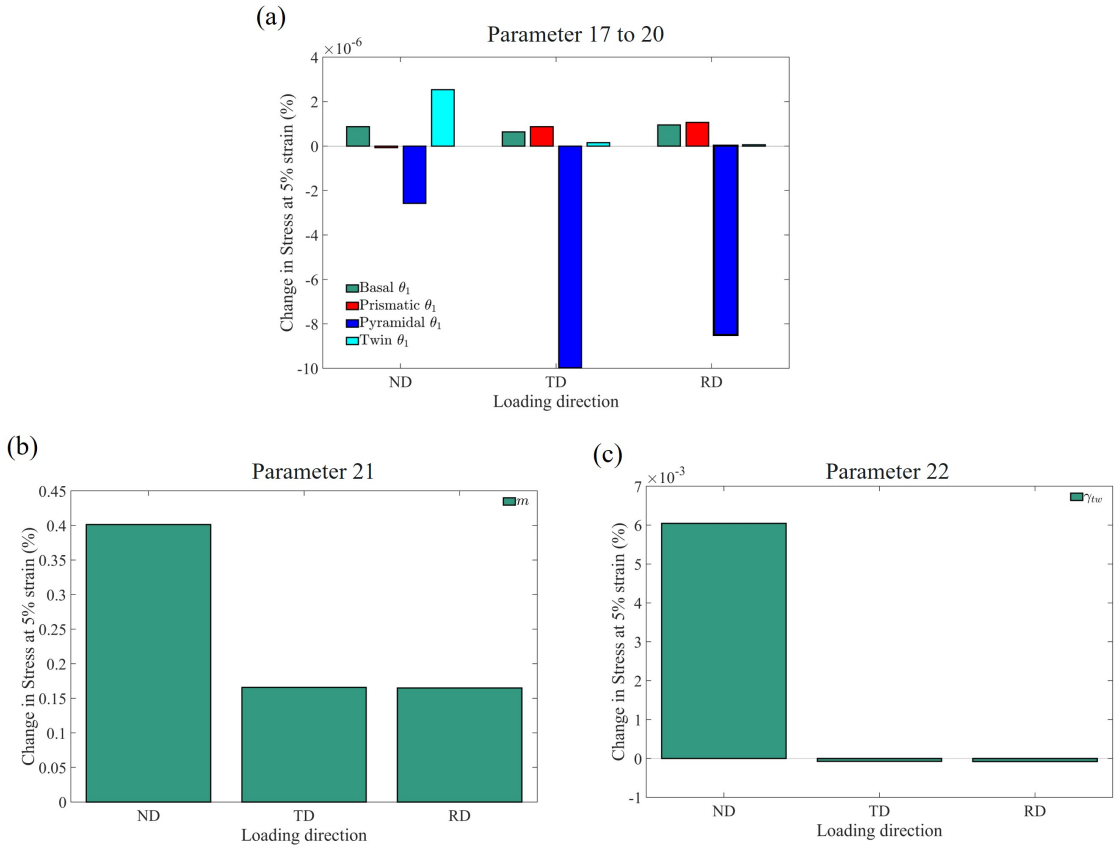

Figure 23: Sensitivity analysis results showing the effect of parameters 17 to 22 on the stress value at 5 % strain of a polycrystal of Zircaloy.

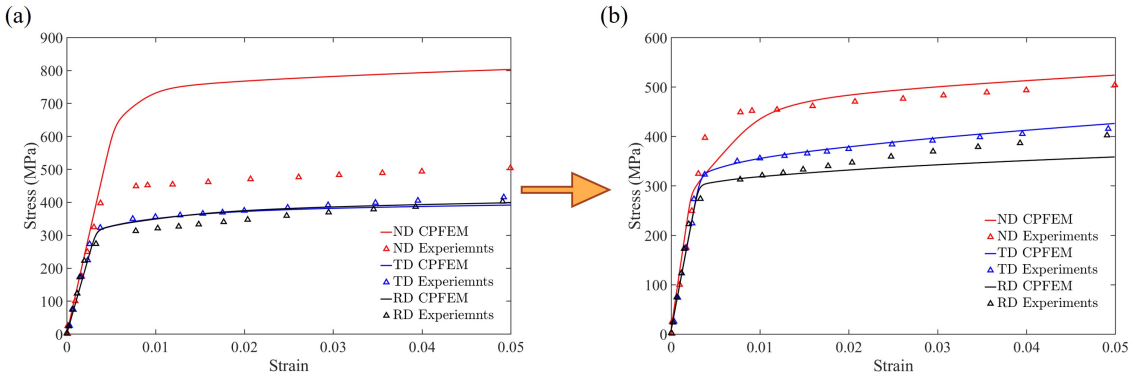

Figure 24: Simultaneous calibration of TD, TD, and RD stress-strain curves for CPFEM model of Zircaloy material.

grain. Time integration of elastoplastic constitutive equations was performed within the child grain. Taylor averaging was used to estimate overall mechanical response. A plain strain compression test using a channel die was simulated for a single crystal of Zircaloy material with the help of implemented

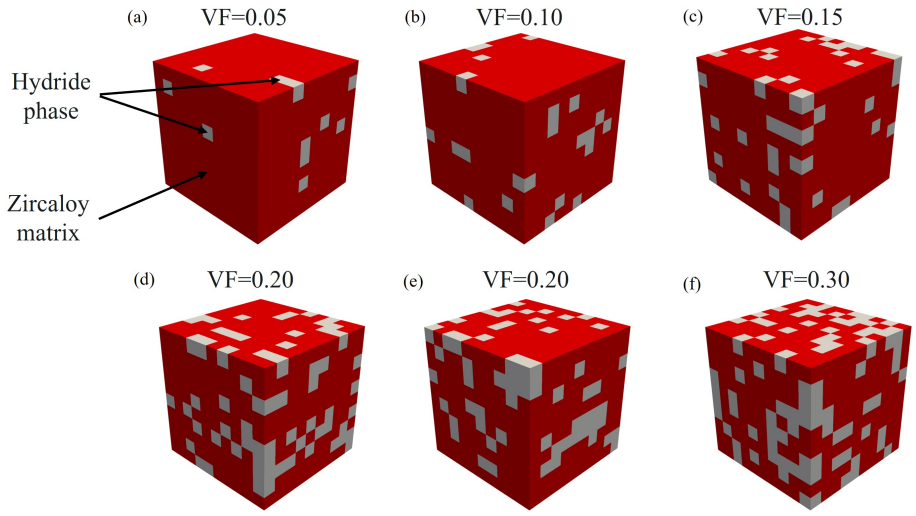

Figure 25: Zircaloy RVE with different volume fraction of hydride phase.

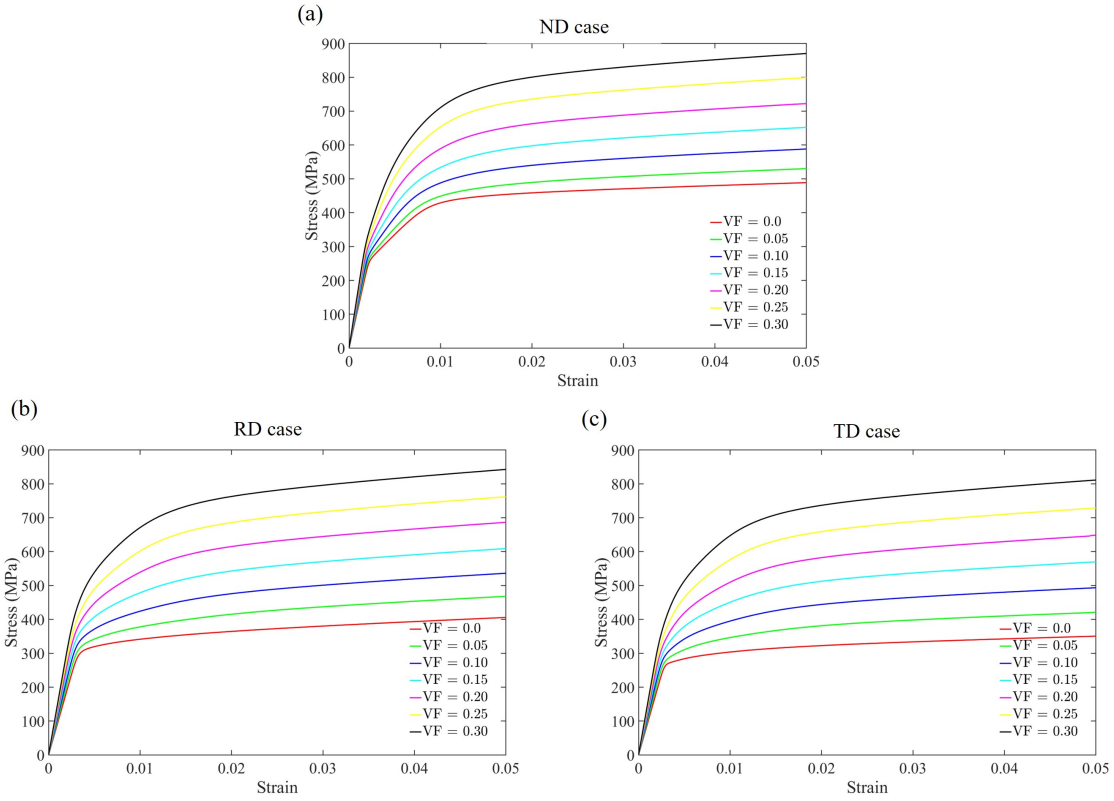

Figure 26: Stress-strain response of RVE along (a) ND, (b) TD, and (c) RD loading for different volume fraction of hydride phase.

CP model. The sample was loaded under five different crystal orientations which facilitated the activation of different slip and twin systems under loading. It was observed that the addition of

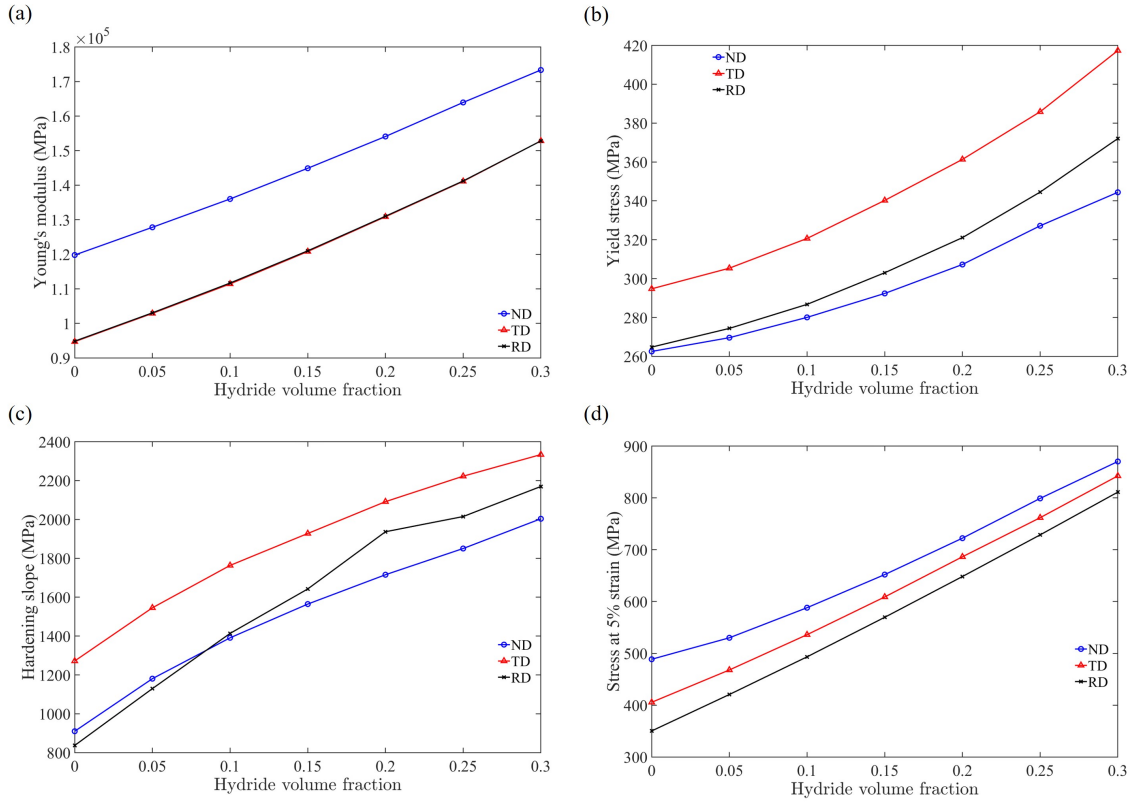

Figure 27: Effect of hydride volume fraction on (a) Young's modulus, (b) yield stress, (c) hardening slope, and (d) stress at 5% strain of RVE.

the twinning model changed the material's response significantly for certain orientations. The highest twinning was observed for case 1 (basal) loading while zero twinning was observed for case 5. Activation of the twin was found to have a further effect on the basal and prismatic slip system activities. An RVE of polycrystalline Zircaloy material was simulated under uniaxial tensile test along ND, TD, and RD loading. The RVE contained 1000 individual grains with strong basal orientation which was observed in experiments. ND orientation had a higher yield with TD and RD with decreasing yields. This trend is in good agreement with experiments conducted by Xu et al. [63]. Twin deformation was found to be negligible in the case of TD and RD orientations.

A sensitivity analysis was conducted of single crystal as well as polycrystal Zircaloy material under different loading conditions to understand the effect of each parameter on the mechanical response of the material and to help the calibration process. All CP model parameters were varied in five steps and uniaxial tensile test response was investigated for Zircaloy material. Calibrated CP material parameters were found for polycrystalline Zircaloy material using experimental stress strain curves in ND, TD, and TD loading with the help of a sensitivity analysis. The results of the sensitivity analysis can be used in the future to develop a convoluted neural network (CNN) which can be used to calibrate

the CP model and obtain material parameters for any HCP material. The use of such a neural network will reduce the time required for calibration while simultaneously increasing the accuracy of the CP model parameters.

The effect of hydride volume fraction on the mechanical behavior of Zircaloy was studied using this newly implemented CP model. It was found that hydride volume fraction plays an important role in the overall mechanical response of the material. Young's modulus, yield stress, hardening slope, and overall stress at 5% strain were found to have a linear relation with hydride volume fraction. The increase in hydride volume fraction by 0.05 led to around 10% increase in Young's modulus, around 5% increase in the yield stress, and around 15% increase in the stress value at the 5% strain. Results obtained from the case study can be used to obtain the homogenized material model for Zircaloy with zirconium hydride which can be used to simulate the response of Zircaloy on the component level. Future work includes the investigation of the effect of temperature on the mechanical properties of Zircaloy and zirconium hydride. This is crucial to study as Zircaloy claddings are exposed to high temperatures.

Acknowledgments

This work was funded by the National Nuclear Security Administration of the US Department of Energy (DOE) through the Tritium Technology Program at Pacific Northwest National Laboratory (PNNL). This research was performed using institutional computing resources at PNNL. PNNL is a multi-program laboratory operated for DOE by the Battelle Memorial Institute under contract no. DE-AC05-76RL01830.

Declaration of Competing Interest

The authors declare that they have no known competing financial interests or personal relationships that could have appeared to influence the work reported in this paper.

Data availability

The data that support the findings of this study are available from the corresponding author upon reasonable request.

References

[1] W. F. Hosford, The mechanics of crystals and textured polycrystals, Oxford University Press (USA) (1993) 248.

[2] U. F. Kocks, C. N. Tomé, H.-R. Wenk, Texture and anisotropy: preferred orientations in polycrystals and their effect on materials properties, Cambridge University Press, 2000.

[3] A. F. Bower, Applied mechanics of solids, CRC press, 2009.

[4] G. I. Taylor, C. F. Elam, Bakerian lecture: the distortion of an aluminium crystal during a tensile test, Proceedings of the Royal Society of London. Series A, Containing Papers of a Mathematical and Physical Character 102 (719) (1923) 643–667.

[5] R. J. Asaro, A. Needleman, Overview no. 42 Texture development and strain hardening in rate dependent polycrystals, Acta Metallurgica 33 (6) (1985) 923–953.

[6] S. S. Kulkarni, T. Truster, H. Das, V. Gupta, A. Soulami, P. Upadhyay, D. Herling, Microstructure-based modeling of friction stir welded joint of dissimilar metals using crystal plasticity, Journal of Manufacturing Science and Engineering 143 (12) (2021).

[7] F. Roters, P. Eisenlohr, L. Hantcherli, D. D. Tjahjanto, T. R. Bieler, D. Raabe, Overview of constitutive laws, kinematics, homogenization and multiscale methods in crystal plasticity finite-element modeling: Theory, experiments, applications, Acta Materialia 58 (4) (2010) 1152–1211.

[8] G. B. Sarma, P. R. Dawson, Texture predictions using a polycrystal plasticity model incorporating neighbor interactions, International Journal of Plasticity 12 (8) (1996) 1023–1054.

[9] C. Miehe, J. Schröder, J. Schotte, Computational homogenization analysis in finite plasticity simulation of texture development in polycrystalline materials, Computer Methods in Applied Mechanics and Engineering 171 (3-4) (1999) 387–418.

[10] O. Diard, S. Leclercq, G. Rousselier, G. Cailletaud, Evaluation of finite element based analysis of 3D multicrystalline aggregates plasticity: Application to crystal plasticity model identification and the study of stress and strain fields near grain boundaries, International Journal of Plasticity 21 (4) (2005) 691–722.

[11] H. Lim, J. Carroll, C. C. Battaile, T. Buchheit, B. Boyce, C. Weinberger, Grain-scale experimental validation of crystal plasticity finite element simulations of tantalum oligocrystals, International Journal of Plasticity 60 (2014) 1–18.

[12] B. Hansen, I. Beyerlein, C. Bronkhorst, E. Cerreta, D. Dennis-Koller, A dislocation-based multi-rate single crystal plasticity model, International Journal of Plasticity 44 (2013) 129–146.

[13] M. Ardeljan, I. J. Beyerlein, B. A. McWilliams, M. Knezevic, Strain rate and temperature sensitive multi-level crystal plasticity model for large plastic deformation behavior: Application to AZ31 magnesium alloy, International Journal of Plasticity 83 (2016) 90–109.

[14] T. Hama, Y. Tanaka, M. Uratani, H. Takuda, Deformation behavior upon two-step loading in a magnesium alloy sheet, International Journal of Plasticity 82 (2016) 283–304.

[15] H. Li, X. Sun, H. Yang, A three-dimensional cellular automata-crystal plasticity finite element model for predicting the multiscale interaction among heterogeneous deformation, DRX microstructural evolution and mechanical responses in titanium alloys, International Journal of Plasticity 87 (2016) 154–180.

[16] P. Baudoin, T. Hama, H. Takuda, Influence of critical resolved shear stress ratios on the response of a commercially pure titanium oligocrystal: crystal plasticity simulations and experiment, International Journal of Plasticity 115 (2019) 111–131.

[17] P. Van Houtte, Simulation of the rolling and shear texture of brass by the taylor theory adapted for mechanical twinning, Acta Metallurgica 26 (4) (1978) 591–604.

[18] S. R. Kalidindi, Incorporation of deformation twinning in crystal plasticity models, Journal of the Mechanics and Physics of Solids 46 (2) (1998) 267–290.

[19] A. Salem, S. Kalidindi, S. Semiatin, Strain hardening due to deformation twinning in α-titanium: Constitutive relations and crystal-plasticity modeling, Acta Materialia 53 (12) (2005) 3495–3502.

[20] H. Abdolvand, M. R. Daymond, C. Mareau, Incorporation of twinning into a crystal plasticity finite element model: Evolution of lattice strains and texture in Zircaloy-2, International Journal of Plasticity 27 (11) (2011) 1721–1738.

[21] M. Ardeljan, R. J. McCabe, I. J. Beyerlein, M. Knezevic, Explicit incorporation of deformation twins into crystal plasticity finite element models, Computer Methods in Applied Mechanics and Engineering 295 (2015) 396–413.

[22] M. Ardeljan, M. Knezevic, Explicit modeling of double twinning in AZ31 using crystal plasticity finite elements for predicting the mechanical fields for twin variant selection and fracture analyses, Acta Materialia 157 (2018) 339–354.

[23] M. Ardeljan, I. J. Beyerlein, M. Knezevic, Effect of dislocation density-twin interactions on twin growth in AZ31 as revealed by explicit crystal plasticity finite element modeling, International Journal of Plasticity 99 (2017) 81–101.

[24] A. Staroselsky, L. Anand, A constitutive model for hcp materials deforming by slip and twinning: application to magnesium alloy AZ31B, International journal of Plasticity 19 (10) (2003) 1843–1864.

[25] S.-B. Yi, C. H. J. Davies, H.-G. Brokmeier, R. Bolmaro, K. U. Kainer, J. Homeyer, Deformation and texture evolution in AZ31B magnesium alloy during uniaxial loading, Acta Materialia 54 (2) (2006) 549–562.

[26] S. R. Agnew, Ö. Duygulu, Plastic anisotropy and the role of non-basal slip in magnesium alloy AZ31B, International Journal of Plasticity 21 (6) (2005) 1161–1193.

[27] S. Graff, W. Brocks, D. Steglich, Yielding of magnesium: From single crystal to polycrystalline aggregates, International Journal of Plasticity 23 (12) (2007) 1957–1978.

[28] B. Xi, G. Fang, Crystal plasticity behavior of single-crystal pure magnesium under plane-strain compression, Rare Metals 36 (2017) 541–549.

[29] J. Cheng, S. Ghosh, Crystal plasticity finite element modeling of discrete twin evolution in polycrystalline magnesium, Journal of the Mechanics and Physics of Solids 99 (2017) 512–538.

[30] J. Cheng, J. Shen, R. K. Mishra, S. Ghosh, Discrete twin evolution in Mg alloys using a novel crystal plasticity finite element model, Acta Materialia 149 (2018) 142–153.

[31] M. Kasemer, P. Dawson, A finite element methodology to incorporate kinematic activation of discrete deformation twins in a crystal plasticity framework, Computer Methods in Applied Mechanics and Engineering 358 (2020) 112653.

[32] M. Yaghoobi, J. E. Allison, V. Sundararaghavan, Multiscale modeling of twinning and detwinning behavior of HCP polycrystals, International Journal of Plasticity 127 (2020) 102653.

[33] M. Yaghoobi, Z. Chen, A. D. Murphy-Leonard, V. Sundararaghavan, S. Daly, J. E. Allison, Deformation twinning and detwinning in extruded Mg-4Al: in-situ experiment and crystal plasticity simulation, International Journal of Plasticity (2022) 103345.

[34] S. Sun, V. Sundararaghavan, A peridynamic implementation of crystal plasticity, International Journal of Solids and Structures 51 (19-20) (2014) 3350–3360.

[35] A. Lakshmanan, J. Luo, I. Javaheri, V. Sundararaghavan, Three-dimensional crystal plasticity simulations using peridynamics theory and experimental comparison, International Journal of Plasticity 142 (2021) 102991.

[36] S. A. Silling, R. B. Lehoucq, Peridynamic theory of solid mechanics, Advances in Applied Mechanics 44 (2010) 73–168.

[37] S. S. Kulkarni, A. Tabarraei, An ordinary state based peridynamic correspondence model for metal creep, Engineering Fracture Mechanics 233 (2020) 107042.

[38] C. J. Permann, D. R. Gaston, D. Andrš, R. W. Carlsen, F. Kong, A. D. Lindsay, J. M. Miller, J. W. Peterson, A. E. Slaughter, R. H. Stogner, R. C. Martineau, Moose: Enabling massively parallel multiphysics simulation, SoftwareX 11 (2020) 100430.

[39] N. Grilli, D. Hu, D. Yushu, F. Chen, W. Yan, Crystal plasticity model of residual stress in additive manufacturing using the element elimination and reactivation method, Computational Mechanics 69 (3) (2022) 825–845.

[40] B. Healy, A. Gullerud, K. Koppenhoefer, A. Roy, S. RoyChowdhury, J. Petti, M. Walters, B. Bichon, K. Cochran, A. Carlyle, WARP3D: 3-D nonlinear finite element analysis of solids for fracture and fatigue processes, University of Illinois at Urbana-Champaign, Urbana-Champaign, IL (2014).

[41] M. Messner, A. Beaudoin, R. Dodds, Consistent crystal plasticity kinematics and linearization for the implicit finite element method, Engineering Computations (2015).

[42] N. Y. Juul, J. Oddershede, A. Beaudoin, K. Chatterjee, M. K. Koker, D. Dale, P. Shade, G. Winther, Measured resolved shear stresses and bishop-hill stress states in individual grains of austenitic stainless steel, Acta Materialia 141 (2017) 388–404.

[43] N. Juul, J. Oddershede, A. Beaudoin, G. Winther, Analysis of inter-and intragranular variations based on 3DXRD data and crystal plasticity, in: IOP Conference Series: Materials Science and Engineering, Vol. 1249, IOP Publishing, 2022, p. 012008.

[44] S. S. Kulkarni, V. Gupta, D. Senor, T. Truster, A. Soulami, R. Devanathan, A microstructure-based modeling approach to predict the mechanical properties of Zr alloy with hydride precipitates, Computational Materials Science 197 (2021) 110654.

[45] S. S. Kulkarni, T. Truster, D. J. Senor, R. Devanathan, A crystal plasticity finite element method modeling of zircaloy with hydride phases based on scanning electron micrographs, in: International Manufacturing Science and Engineering Conference, Vol. 85819, American Society of Mechanical Engineers, 2022, p. V002T05A002.

[46] M. Yaghoobi, S. Ganesan, S. Sundar, A. Lakshmanan, S. Rudraraju, J. E. Allison, V. Sundararaghavan, Prisms-plasticity: An open-source crystal plasticity finite element software, Computational Materials Science 169 (2019) 109078.

[47] R. Quey, M. Kasemer, The neper/fepx project: Free/open-source polycrystal generation, deformation simulation, and post-processing, in: IOP Conference Series: Materials Science and Engineering, Vol. 1249, IOP Publishing, 2022, p. 012021.

[48] R. Quey, P. Dawson, F. Barbe, Large-scale 3D random polycrystals for the finite element method: Generation, meshing and remeshing, Computer Methods in Applied Mechanics and Engineering 200 (17-20) (2011) 1729–1745.

[49] C. Geuzaine, J.-F. Remacle, Gmsh: A 3-D finite element mesh generator with built-in pre-and post-processing facilities, International Journal for Numerical Methods in Engineering 79 (11) (2009) 1309–1331.

[50] J. Lu, W. Sun, A. Becker, Material characterisation and finite element modelling of cyclic plasticity behaviour for 304 stainless steel using a crystal plasticity model, International Journal of Mechanical Sciences 105 (2016) 315–329.

[51] A. Chakrabarty, P. Chakraborty, V. K. Sahu, N. P. Gurao, N. Khutia, Investigation of strain localization in additively manufactured AlSi10Mg using CPFEM, in: Composite Materials for Extreme Loading, Springer, 2022, pp. 199–214.

[52] H. Lim, C. C. Battaile, J. E. Bishop, J. W. Foulk III, Investigating mesh sensitivity and polycrystalline rves in crystal plasticity finite element simulations, International Journal of Plasticity 121 (2019) 101–115.

[53] W. G. Feather, H. Lim, M. Knezevic, A numerical study into element type and mesh resolution for crystal plasticity finite element modeling of explicit grain structures, Computational Mechanics 67 (1) (2021) 33–55.

[54] F. Xu, R. Holt, M. Daymond, Modeling lattice strain evolution during uniaxial deformation of textured Zircaloy-2, Acta Materialia 56 (14) (2008) 3672–3687.

[55] V. Tvergaard, A. Needleman, Analysis of the cup-cone fracture in a round tensile bar, Acta Metallurgica 32 (1) (1984) 157–169.

[56] E. Kelley, W. Hosford, Plane-strain compression of magnesium and magnesium alloy crystals, Trans Metall Soc AIME 242 (1968) 5–13.

[57] Y. Liang, S. Jiang, Y. Zhang, C. Zhao, Effect of plane strain compression and subsequent recrystallization annealing on microstructures and phase transformation of NiTiFe shape memory alloy, Journal of Materials Engineering and Performance 27 (9) (2018) 4514–4524.

[58] E. Fisher, C. Renken, Single-crystal elastic moduli and the hcp→ bcc transformation in Ti, Zr, and Hf, Physical Review 135 (2A) (1964) A482.

[59] O. Nassif, T. J. Truster, R. Ma, K. B. Cochran, D. M. Parks, M. C. Messner, T. Sham, Combined crystal plasticity and grain boundary modeling of creep in ferritic-martensitic steels: I. Theory and implementation, Modelling and Simulation in Materials Science and Engineering 27 (7) (2019) 075009.

[60] M. Knezevic, B. Drach, M. Ardeljan, I. J. Beyerlein, Three dimensional predictions of grain scale plasticity and grain boundaries using crystal plasticity finite element models, Computer Methods in Applied Mechanics and Engineering 277 (2014) 239–259.

[61] F. Xu, R. Holt, M. Daymond, R. Rogge, E. Oliver, Development of internal strains in textured Zircaloy-2 during uni-axial deformation, Materials Science and Engineering: A 488 (1-2) (2008) 172–185.

[62] M. A. Groeber, M. A. Jackson, DREAM3D: A digital representation environment for the analysis of microstructure in 3D, Integrating Materials and Manufacturing Innovation 3 (1) (2014) 56–72.

[63] F. Xu, R. Holt, M. Daymond, Modeling texture evolution during uni-axial deformation of Zircaloy-2, Journal of Nuclear Materials 394 (1) (2009) 9–19.

[64] D. O. Northwood, The development and applications of zirconium alloys, Materials & Design 6 (2) (1985) 58–70.

[65] R. Konings, R. E. Stoller, Comprehensive nuclear materials, Elsevier, 2020.

[66] A. T. Motta, A. Yilmazbayhan, M. J. G. da Silva, R. J. Comstock, G. S. Was, J. T. Busby, E. Gartner, Q. Peng, Y. H. Jeong, J. Y. Park, Zirconium alloys for supercritical water reactor applications: Challenges and possibilities, Journal of Nuclear Materials 371 (1-3) (2007) 61–75.

[67] T. Allen, J. Busby, M. Meyer, D. Petti, Materials challenges for nuclear systems, Materials Today 13 (12) (2010) 14–23.

[68] A. T. Motta, L. Capolungo, L.-Q. Chen, M. N. Cinbiz, M. R. Daymond, D. A. Koss, E. Lacroix, G. Pastore, P.-C. A. Simon, M. R. Tonks, B. Wirth, M. Zikry, Hydrogen in zirconium alloys: A review, Journal of Nuclear Materials 518 (2019) 440–460.

[69] S. Ziaei, M. Zikry, How semi-coherent bcc hydride interfacial interactions affect the inelastic deformation and fracture behavior of hcp zirconium alloys, Mechanics of Materials 130 (2019) 1–8.

[70] J.-H. Huang, S.-P. Huang, Effect of hydrogen contents on the mechanical properties of Zircaloy-4, Journal of Nuclear Materials 208 (1-2) (1994) 166–179.

[71] H.-M. Tung, T.-C. Chen, C.-C. Tseng, Effects of hydrogen contents on the mechanical properties of Zircaloy-4 sheets, Materials Science and Engineering: A 659 (2016) 172–178.

Appendix A. Summary of code changes to WARP3D

This section provides a brief overview of the changes in the source code of WARP3D to incorporate twinning along with slip activity in HCP metals. As of the current report, only HCP18 is considered with the twinning. The text in red refers to variables and data structures, the text in brown refers to subroutine names, and the text in blue refers to files (fortran codes or otherwise).

Adjustments to crystal data structures:

- Additions to type :: crystal_properties in include_sig_up and type :: crystal_props and type :: crystal in mod_crystals.f

  1. n_twin_slip - integer to indicate number of slip systems in child grain - set to hcp18,
  2. twinning - logical to indicate whether twinning is considered or not (only works with slip_type = hcp24_t or hcp24_c),
  3. gamma_tw = real; γ_0^{tw} twinning shear

- Additions to type :: crystal_state in mod_crystals.f

  1. twinned - integer to indicate whether twinning has initiated in parent grain,
  2. child - integer to indicate whether the we're performing the time-integration of elasto-plastic constitutive equations for the parent (0) or child (1) grain ,

Addition of extended Voche hardening law

These parameters are used to define the matrices and partial derivatives necessary for time integration of elasto-plastic constitutive equations, as defined in Eqns. 2, 7 - 10. Note that the subroutines that define these terms are called repeatedly. These subroutines are added to the switch case for the variable h_type=10 following every occurrence of the comment line `c ***** START: Add new Constitutive Models into this block *****`

Adjustments to subroutines

- Modifications to mod_crystals.f

  1. In module crystal_data, initialize_new_crystal, added two variables a_hcp and c_hcp to customize the lattice parameters of hcp crystal structures

Quantity	Variable	Units
$\dot{\gamma}_0$ (basal)	cp_001	s^{-1}
$\dot{\gamma}_0$ (prismatic)	cp_002	s^{-1}
$\dot{\gamma}_0$ (pyramidal <c+a>)	cp_003	s^{-1}
$\dot{\gamma}_0$ (twinning)	cp_004	s^{-1}
g_0 (basal)	cp_005	MPa
g_0 (prismatic)	cp_006	MPa
g_0 (pyramidal <c+a>)	cp_007	MPa
g_0 (twinning)	cp_008	MPa
g_1 (basal)	cp_009	MPa
g_1 (prismatic)	cp_010	MPa
g_1 (pyramidal <c+a>)	cp_011	MPa
g_1 (twinning)	cp_012	MPa
θ_0 (basal)	cp_013	MPa
θ_0 (prismatic)	cp_014	MPa
θ_0 (pyramidal <c+a>)	cp_015	MPa
θ_0 (twinning)	cp_016	MPa
θ_1 (basal)	cp_017	MPa
θ_1 (prismatic)	cp_018	MPa
θ_1 (pyramidal <c+a>)	cp_019	MPa
θ_1 (twinning)	cp_020	MPa
m	cp_021	(none)

Table A.3: Parameter to variable map for extended Voche hardening in WARP3D.

2. In module crystal_data, finalize_new_crystal, added two new slip types: hcp24_t for tensile twinning and hcp24_c for compressive twinning with slip_type=11 and slip_type=12 respectively.
3. Added module twin_variants: Calculate the twin reflection tensors for all variants and store in reflection_twins_t or reflection_twins_c for tensile and compressive twins respectively

- Modifications to incrystal.f
  - In incrystal,
    1. added two new slip types: hcp24_t for tensile twinning and hcp24_c for compressive twinning with slip_type=11 and slip_type=12 respectively.

2. added line to read γ_0^{tw}: gamma_tw
3. added hardening type avoche with h_type=10

- Modifications to param_def
  - Added max_twin_sys=18
- Modifications to mm10_a.f
  - In mm10_set_cons, added switch case (h_type=10) for extended Voche hardening model. The variable process_G_H to include the new hardening model
  - Added mm10_a_dim2_dim1 to swap between second rank tensors and vectors, and mm10_a_dim4_dim2 to swap between 4th rank tensors and 6x6 matrices, based on flag = 0 (for decrease in dimension)/ 1 (for increase in dimension)
  - Added mm10_a_rotate_4th and mm10_a_rotate_2nd to rotate 4th and 2nd rank tensors respectively, based on q = rotation matrix
  - Added mm10_a_transpose for transposing a m,n matrix
  - Added mm10_init_cc_props_twin
    1. Inputs: inc_props: crystal_props for parent grain, variant : integer indicating most active twin variant
    2. Outputs: cc_props: crystal_props for child grain
    3. Rotates inc_props%stiffness,inc_props%ms and inc_props%qs by q=reflection_twin(variant) and returns cc_props%stiffness, cc_props%ms, and cc_props%qs respectively
    4. cc_props%slip_type=10 (HCP18)
  - Added mm10_a_tt_inc_twin to shut off other twin variants after twin has initiated by setting tt(# ≠ variant) = 1.0e3*tt(# ≠ variant)
  - Added mm10_init_avoche to initialize the CRSS values of extended Voche hardening model (refer to Table A.3)
  - Added mm10_setup_avoche to initialize the first user variable to be equal to the current time
  - Added mm10_init_cc_hist_twin0: Subroutine to set the history vectors for keeping track of twin state variables; uses the time-step n crystal_state of the parent grain. Invoked **only once** when the total twin volume fraction ($\sum_\beta f_\beta$) exceeds 2%.

1. Alters the crystal orientation of the twin/child crystal_state according to $\boldsymbol{R}^e$ = elastic rotation tensor.
2. Sets the history vectors as described in section 3: the stress state ($\boldsymbol{t}$), the stretching tensor ($\boldsymbol{D}$), the accumulated plastic strain ($\int \sqrt{\frac{2}{3}\bar{\boldsymbol{d}}^p : \bar{\boldsymbol{d}}^p dt}$) are set to the same values as the parent grain at inception; both the CRSS values and the current time-rate of evolution of CRSS values (tt_rate = $\dot{g}^\alpha$) is set to be the same as the slip systems in the parent grain
3. Note that the number of slip systems is reduced to 18

– Added mm10_copy_cc_hist_twin: copies the history vector for the child into corresponding the time-step n crystal_state.

1. The copy subroutine is called regardless of whether the twin has just initiated or not
2. A previous call to mm10_init_cc_hist_twin0 ensures that the history vectors are set appropriately.
3. As the previously initiated twin grows in size, the converged state variables for time-step $n+1$ are stored in appropriate history vector locations

– Added mm10_setup_np1_twin : setup the time-step $n+1$ crystal_state for the child grain; same as mm10_setup_np1 except it uses the time-step n crystal_state and crystal_props structs for the child grain instead.

– Added mm10_store_cryhist_twin: store the updated $n+1$ crystal_state for the child grain into appropriate history locations as defined in mm10_d.f

- Modifications to mm10_b.f - several subroutines are added to mm10_b.f to define the partial derivatives necessary to incorporate anisotropic voche hardening with the hcp18/hcp24_t/ hcp24_c crystal structures.

– Added mm10_v_avoche.f to return the vectors vec1(N^s) = $\Delta\gamma^i|_{i=1}^{N^s}$ and vec2 = *None* that are used repeatedly in other subroutines to define the partial derivatives necessary

– Added mm10_a_avoche.f to return the vectors arr1(N^s) = $\frac{\partial \Delta\gamma^i}{\partial \tau^i}|_{i=1}^{N^s}$ and arr2(N^s, N^{hard}) = $\frac{\partial \Delta\gamma^i}{\partial g^j}|_{i=1,j=1}^{N^s,N^{hard}}$ that are used repeatedly in other subroutines to define the partial derivatives necessary

– Added mm10_slipinc_avoche.f to return the slip increment for slip system $\alpha \Rightarrow \Delta\gamma^\alpha$ (see Eq.(2))

– Added mm10_h_avoche.f, mm10_estress_avoche.f, mm10_ehard_avoche.f - returns g^α_{n+1}, $\frac{\partial g^\alpha_{n+1}}{\partial \boldsymbol{t}}$, and $\frac{\partial g^\alpha_{n+1}}{\partial g^\beta_{n+1}}$ respectively (Refer Eqs. (9))

Crystal vector index	Length	Quantity (child grain)
12	6	$\boldsymbol{\sigma}$(Stress)
13	3	$\boldsymbol{g}$ (Euler angles)
14	9	$\boldsymbol{R}^p$ (Plastic Rotation tensor)
15	6	$\Delta\bar{\boldsymbol{d}}$ (Unrotated Strain increment)
16	6	$\boldsymbol{V}^e$ (elastic lattice stretch tensor)
17	n_twin_slip	$\Delta\gamma^\alpha$
18	n_twin_slip	g^α
19	n_twin_slip	$\dot{g}^\alpha$
20	6	$\boldsymbol{\varepsilon}^d$
21	6	$\boldsymbol{\varepsilon}^h$
22	1	twinned

Table A.4: Extended history vector to account for crystal state evolution in the child grain

  - Added mm10_dgdt_avoche.f - returns $\frac{\partial \Delta\gamma^i}{\partial \tau^i}|_{i=1}^{N^s}$
  - Added mm10_dgdh_avoche.f - returns $\frac{\partial \Delta\gamma^i}{\partial g^j}|_{i=1,j=1}^{N^s,N^{hard}}$

- Modifications to mm10_d.f - The history vector length and the number of per-crystal terms are adjusted to include the twin volume fraction evolution and accommodate the time-step n crystal_state for the child grain.
  - Crystal history vector index length (length_crys_hist) is increased from 12-22.

- Modifications to mm10_e.f
  - Added mm10_avoche_GH - To calculate the latent hardening matrix for anisotropic Voche hardening law ($q^{\alpha\beta}$)

Adjustments to algorithm

The mm10_a_do_crystal subroutine in mm10_a.f contains the lines necessary to call the other subroutines to update the crystal state from time-step n to $n+1$. We describe the algorithmic modifications necessary to incorporate twinning into the existing update codes in Algorithm 1.

Algorithm 1 Algorithm to include twinning in WARP3D

Require: crystal History $(\boldsymbol{\sigma}_n, g_n^\alpha, \dot{g}_n^\alpha, \boldsymbol{\varepsilon}_n^p, \boldsymbol{V}_n^e)$, $\boldsymbol{R}, \nabla \boldsymbol{F}^e$

Unchanged: call mm10_solve_crystal for parent grain

max_f_twin, max_twin_id$\leftarrow \max f_\beta|_{\beta=1}^{N_{tw}}, \leftarrow \arg\max f_\beta|_{\beta=1}^{N_{tw}}$

if max_f_twin ≥ 0.02 && max_f_twin ≤ 0.9 **then**

if twinned == 1 **then**

call mm10_init_cc_props_twin

call mm10_a_tt_inc_twin

call mm10_init_cc_hist_twin0

call mm10_copy_cc_hist_twin

call mm10_setup_np1_twin

call mm10_solve_crystal (for child grain)

else if twinned == 2 **then**

call mm10_init_cc_props_twin

call mm10_copy_cc_hist_twin

call mm10_setup_np1_twin

call mm10_solve_crystal (for child grain)

end if

end if

if twinned == 1 **or** twinned == 2 **then**

$$\begin{aligned} \Delta\boldsymbol{\sigma} &= \left(1 - \sum_{\beta=1}^{N^{tw}} f^\beta\right) \Delta\boldsymbol{\sigma}^{pa} + \sum_{\beta=1}^{N^{tw}} f^\beta \Delta\boldsymbol{\sigma}^{ch} + \sum_{\beta=1}^{N^{tw}} \Delta f^\beta (\boldsymbol{\sigma}^{ch} - \boldsymbol{\sigma}^{pa}) \\ \boldsymbol{J} &= \left(1 - \sum_{\beta=1}^{N^{tw}} f^\beta\right) \boldsymbol{J}^{pa} + \sum_{\beta=1}^{N^{tw}} f^\beta \boldsymbol{J}^{ch} + \sum_{\beta=1}^{N^{tw}} \Delta f^\beta (\boldsymbol{J}^{ch} - \boldsymbol{J}^{pa}) \end{aligned} \tag{A.1}$$

else

$$\begin{aligned} \Delta\boldsymbol{\sigma} &= \Delta\boldsymbol{\sigma}^{pa} \\ \boldsymbol{J} &= \boldsymbol{J}^{pa} \end{aligned} \tag{A.2}$$

end if